Injectable collagen scaffold enables long-distance neural repair after spinal cord injury in canines

Authors: Haoxuan Huang[1,6,†], Tianqian Shen[1,6,†], Bin Dai[4], Lei Wang[1,5,6], Weidong Liu[1,5,6], Zhaoping Wu[1,7], Yudong Cao[1,6], Wen Yin[1,6], Juan Li[1,6], Wenlong Zhang[1,6], Caiping Ren[1,5,6,*], Yannan Zhao[2,3,*], Jianwu Dai[3,*], Xingjun Jiang[1,6,*]

Affiliations:

1 Department of Neurosurgery, Xiangya Hospital, Central South University, Changsha, Hunan, 410008, China.

2 Institute of Clinical Medical Sciences, China-Japan Friendship Hospital, Beijing, 100029, China.

3 Laboratory of Integrative Physiology, Institute of Genetics and Developmental Biology, Chinese Academy of Sciences, Beijing, 100080, China.

4 DB Wuderegen Biomedical Technologies Co., Ltd, Zhenjiang, 212009, China.

5 NHC Key Laboratory of Carcinogenesis, The Key Laboratory of Carcinogenesis and Cancer Invasion of the Chinese Ministry of Education, Cancer Research Institute, Xiangya School of Basic Medical Science, Central South University, Changsha, Hunan, 410078, China.

6 National Clinical Research Center for Geriatric Diseases, Xiangya Hospital, Central South University, Changsha, Hunan, 410008, China.

7 Department of Neurosurgery, The Second Affiliated Hospital of Harbin Medical University, Harbin, 150086, China.

† Haoxuan Huang and Tianqian Shen have contributed equally to this work.

***Corresponding Authors:**

Caiping Ren (E-mail: rencaiping@csu.edu.cn), Yannan Zhao (E-mail: ynzhao@genetics.ac.cn), Jianwu Dai (E-mail: jwdai@genetics.ac.cn), Xingjun Jiang (E-mail: jiangxj@csu.edu.cn)

Keywords: extracellular matrix, spinal cord injury, axon regeneration, microglia, microenvironment

Abstract:

Rationale: Spinal cord injury (SCI) causes irreversible neurological deficits, and long-distance axon regeneration across extensive tissue defects remains a major therapeutic challenge. Here, we developed an extracellular matrix-derived injectable collagen scaffold (INCS) that can be stored at room temperature, rapidly reconstituted with

saline, and self-assembled into an ordered porous network suitable for filling irregular spinal cord lesions.

Methods: INCS was synthesized and characterized for the microstructure and rheological properties. In a canine model of 25 mm thoracic hemisection SCI, therapeutic effects of INCS implantation were evaluated, including locomotor recovery, electroneurographic signal conduction, fiber tract reconstruction, bladder function and biocompatibility. Histological analyses revealed axon regeneration, neuroinflammation, scarring, angiogenesis and local neural conduction. Single-nucleus RNA sequencing elucidated repair mechanisms, identifying key targets and pathways.

Results: INCS implantation showed excellent in vivo biocompatibility without systemic toxicity, organ injury, infection, or evident foreign body response. INCS integrated with host tissue, reduced glial and fibrotic scarring, attenuated chronic inflammation, promoted vascular remodeling, and preserved the lesion microenvironment. Functionally, INCS significantly improved locomotor recovery, enhanced cortical motor-evoked potential conduction, alleviated bladder dysfunction, and reduced denervation-associated muscle atrophy. Histological analyses demonstrated axon regeneration and remyelination across the lesion, accompanied by reconstruction of structural continuity. Single-nucleus RNA sequencing further revealed that INCS reshaped the cellular landscape and activated pro-regenerative neuron–microglia communication.

Conclusions: Overall, as a clinically translatable, ready-to-use biomaterial, INCS expanded reparative $Fmn1^{+}$ and $Spp1^{+}$ microglial states associated with axon guidance, extracellular matrix remodeling, synaptic organization, and MAPK/PI3K-AKT signaling. These findings establish INCS as a preclinically promising biomaterial for promoting long-distance spinal cord repair.

Introduction

Spinal cord injury (SCI) remains one of the most intractable challenges in medicine, causing severe and permanent disability along with immense psychological trauma and economic strain [1]. Spinal cord is a highly organized and bilaterally symmetric structure. Crush or transection will disrupt long-projecting ascending and descending tracts and result in loss of motor, sensory, and autonomic function below the lesion [2]. Traumatic SCI typically extends well beyond the initial impact site, as secondary insults such as ischemia and edema propagate damage over far greater distances. We previously reported that approximately 80% of patients with spinal cord transection harbor lesions longer than 2 cm, indicating that the majority of clinical cases involve extensive tissue loss [3, 4]. Given the extremely limited intrinsic regenerative capacity of adult neurons, achieving axonal regeneration across such distances remains a major challenge in spinal cord repair [5]. SCI initiates a cascade of pathophysiological processes, including ischemia, edema, neuronal death, inflammatory activation, excitotoxicity, and scar formation, which evolve temporally and spatially to create a profoundly heterogeneous microenvironment at the lesion site [6-8]. Consequently, strategies aimed at reshaping the injury microenvironment represent a promising route to restore tissue homeostasis and support neural regeneration.

Biomaterials have emerged as versatile tools for remodeling the hostile SCI microenvironment [9]. By filling tissue defects and cystic cavities, biomaterials can restore structural continuity, attenuate scar formation and inflammation, and provide a permissive substrate for cell migration and axon extension [10-12]. Among the diverse library of natural and synthetic polymers tested, extracellular matrix (ECM)-derived materials have attracted particular attention. ECM includes the structural architecture and molecular composition of native tissues, such as collagens, glycosaminoglycans, growth factors, and bioactive peptide motifs, which can recapitulate the biomechanical cues of endogenous niches for tissue regeneration [13, 14]. In SCI models, ECM-derived materials have been reported to modulate the immune response, recruit endogenous neural progenitors, and support axon growth [15-17].

Nevertheless, the clinical translation of ECM is hampered by practical shortcomings [18]. Existing ECM-derived materials are often derived from variable tissue sources with considerable batch-to-batch variability, leading to inconsistent therapeutic efficacy. Most products are configured as pre-formed scaffolds that do not readily adapt to the irregular shapes of traumatic lesions, complicating intraoperative handling [19, 20]. Injectable ECM-derived hydrogels have been introduced to achieve conformal filling of the injury site, but they are typically difficult to prepare and dependent on low-temperature storage and transport [16, 21]. Loss of the preservation condition rapidly

degrades their mechanical properties and bioactivity [18]. These constraints effectively restrict ECM-based therapies to well-equipped hospitals and elective procedures, excluding them from acute trauma settings or resource-limited environments where most of SCI patients reside.

To facilitate the broader use of ECM-derived materials, we developed an injectable collagen scaffold (INCS) that is easy to store, prepare, and apply clinically. Through defatting, decellularization, lyophilization, and cryogenic milling of bovine tissue, we produced microparticles that are stable at room temperature while preserving matrix composition. These particles can be stored and transported in sterile containers without refrigeration and reconstituted intraoperatively by suspension in saline. After standing at room temperature, the suspension becomes viscous and injectable. Notably, the reconstituted microparticles self-assemble into a fibrous network without added initiators, generating a scaffold with relatively uniform pores, ordered organization, and rheological properties suitable for filling lesions of complex geometry.

In this study, we systematically evaluated the reparative effects of INCS in a canine large-animal model of SCI. We found that INCS integrated well with host tissue, remodeled the injury site microenvironment, and improved neurological recovery. We further uncovered a microglia-mediated mechanism that coordinates neural repair. Most importantly, INCS enables long-distance axon regeneration across the lesion—a finding that is unprecedented **(Figure 1)**. In summary, our study provides an injectable microparticle-assembled ECM scaffold that overcomes key practical barriers of existing biomaterials and paves the way toward clinical application for SCI and potentially other neurological disorders.

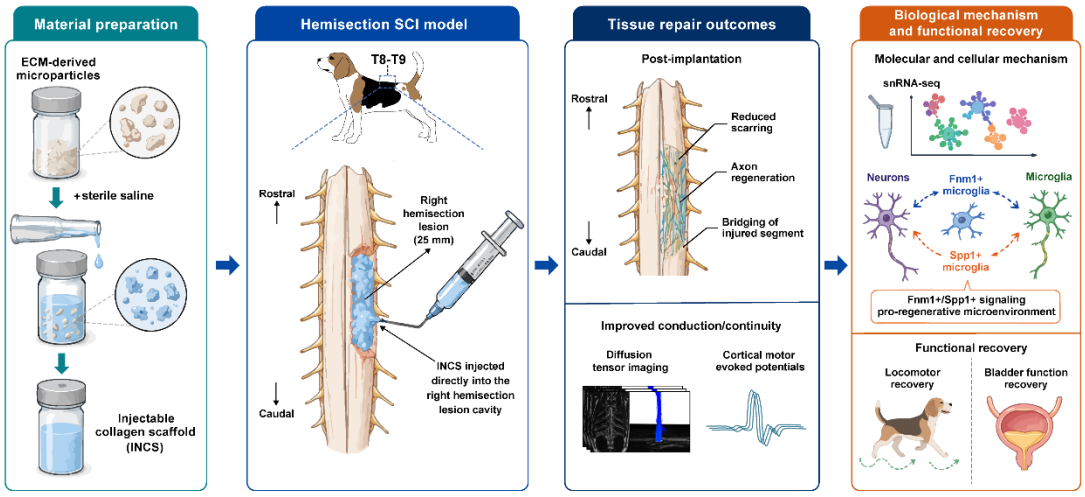


Figure 1. Schematic illustration of SCI repair by INCS. An ECM-derived injectable, self-assembling collagen scaffold is applied in a preclinical canine model of long-distance (25 mm) hemisection SCI. INCS treatment enhances electrophysiological conduction and leads to recovery of bladder and motor function. Mechanistic analyses further delineate the heterogeneity of the injury

site microenvironment and the molecular pathways underlying axonal regeneration.

Results

Preparation and characterization of INCS

INCS was prepared in powder form and reconstituted before use. Sterile saline was added to each vial and vortexed to obtain a uniform suspension. The mixture was left undisturbed for one hour prior to injection into the spinal cord lesion site **(Figure 2A-B)**. Scanning electron microscope images of INCS after lyophilization showed that it formed a distributed, ordered and porous network structure by the self-assembly of dispersed collagen fibrils into a supportive three-dimensional framework **(Figure 2C)**. Proteomic analysis revealed that INCS consists predominantly of collagen types I and III **(Figure S1A)**. To evaluate decellularization efficacy, residual DNA content was quantified. The results showed a low residual DNA content of 3.73 ± 1.09 ng/mg, indicating effective removal of cellular DNA from INCS. Meanwhile, quantitative analysis of scanning electron microscope images revealed that the INCS exhibited an average pore size of 107.34 ± 3.24 μm **(Figure 2D)**. Previous studies have suggested that scaffold pores ranging from 22 to 200 μm are optimal for allowing nerve fibers to penetrate the matrix [22, 23]. Consequently, such a pore diameter favors axonal outgrowth, as well as the migration and adhesion of endogenous cells. The rheological properties of INCS demonstrated a shear-thinning effect. As the angular frequency increased from 0.1 to 100 rad s^{-1}, the viscosity decreased markedly from 8907.6 to 16.9 Pa·S **(Figure 2E)**. Meanwhile, the storage modulus (G′) stayed steadily above the loss modulus (G″) **(Figure 2F)**. These structural properties support the injectability of INCS and indicate that the internal scaffold architecture remains stable during injection. Subsequently, the time-dependent stability of INCS was evaluated under a constant frequency of 1.0 Hz and a strain of 1.0% **(Figure 2G)**. The G′ and G″ of INCS were 981.16 ± 6.29 Pa and 181.78 ± 0.56 Pa, respectively, which align with the rheological properties of native spinal cord tissue [24, 25]. Strain sweep measurements showed that the G′ and G″ of INCS remained stably unchanged between 0.1% and 10% strain. At a strain of approximately 30-40%, the G′ and G″ curves crossed, and beyond this crossover point G″ exceeded G′ (**Figure 2H**). These results demonstrate that INCS exhibits favorable rheological properties, compatible with spinal cord tissue.

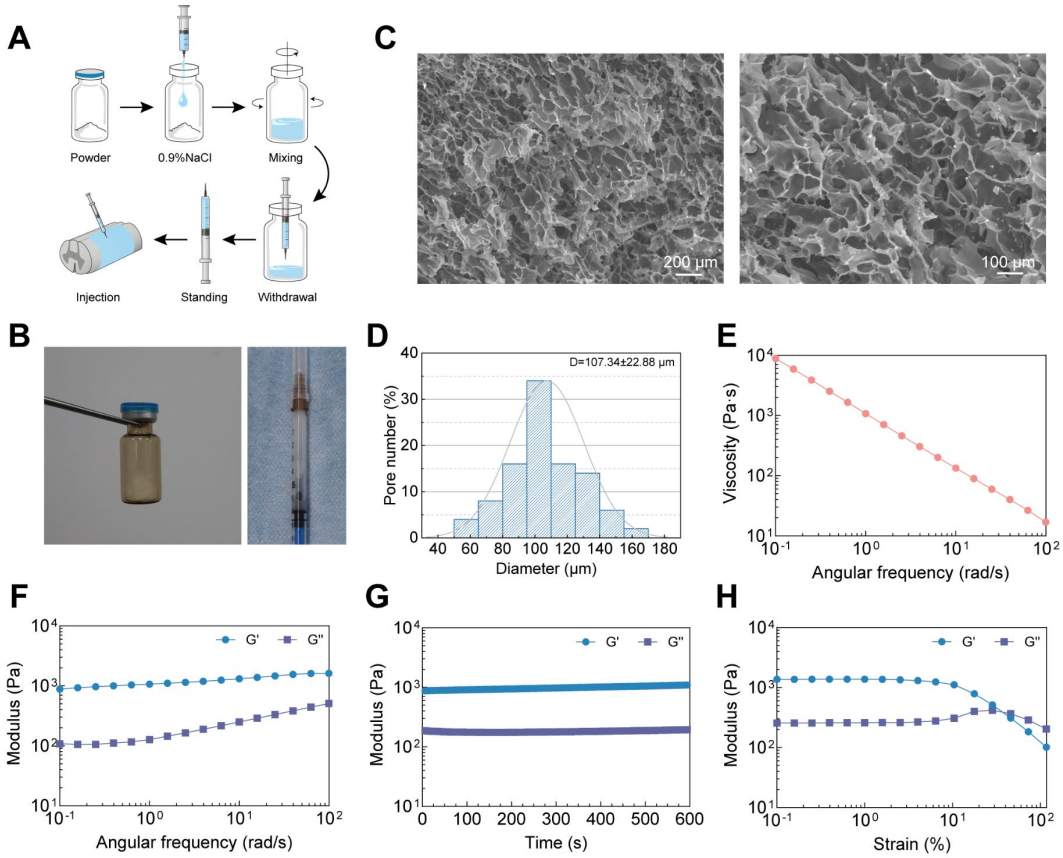


Figure 2. Preparation and characterization of INCS. (A) Schematic diagram of the procedure for injecting INCS into the spinal cord injury site. (B) Dissolved powder self-assembled into a gel-like matrix upon standing. (C) Transverse scanning electron microscope micrographs of lyophilized INCS (Scale bar = 200 μm, zoomed-in views scale bar = 100 μm). (D) The pore-sized distribution and average pore diameter of INCS. (E, F) Rheological tests of viscosity characteristic (E) as well as storage and loss moduli (G′ and G″) for INCS in frequency-sweep (F). (G) Time sweep of G′ and G″ for INCS at 1% strain and a frequency of 1 Hz. (H) Strain sweep of INCS from 0.1% to 100% at fixed angular frequency ω = 10 rad/s.

Establishment of long-distance hemisection canine SCI model for INCS implantation

Our previous work has established the canine as a clinically relevant model for SCI, closely recapitulating the pathophysiology of the human central nervous system [26-30]. Complete spinal cord transection was associated with high mortality, frequent pressure ulcers, and other postoperative complications [31, 32]. To balance animal welfare considerations with the need for a robust demonstration of therapeutic efficacy, we adopted a 25 mm hemisection model. This approach preserves one side of the spinal cord, thereby mitigating severe complications, while creating a long-segment defect that enables the assessment of therapeutic outcomes of INCS. The schematic overview of study is presented in **Figure 3A**. Twelve animals underwent right-sided spinal cord hemisection at the T8-T9 level, with a 25 mm segment excised to create the lesion

(Figure 3B). The INCS was administered into the lesion gap in six animals, leaving the remaining six as injury controls. This material allowed complete defect filling and intimate integration with the host tissue **(Figure 3B)**. The dura was sutured to protect the lesion site and prevent cerebrospinal fluid leakage. Postoperative management involved antibiotic prophylaxis, wound care, daily assisted urination, and protective measures against pressure ulcers. Following injury, the right pelvic limb was immediately paralyzed, with loss of voluntary movement and weight-bearing. Bilateral pelvic limb paralysis occurred in a subset of canines. However, the contralateral hindlimb recovered voluntary movement and weight-bearing after a transient spinal shock. All canines maintained stable vital signs and general condition throughout the observation period, suggesting that the INCS was compatible *in vivo*. Nerve regeneration was comprehensively assessed through functional, imaging, histopathological, and single-cell sequencing. Detailed information for each canine experimented in this study covering weight changes, systemic complications, survival time, and analyses performed is provided in **Table S1-S2**.

INCS enhanced locomotion recovery and attenuated denervation-associated muscle atrophy after SCI

Six months after implantation, dissection revealed local scar formation at the surgical site in both the CTRL and INCS groups, with no signs of infection or necrosis. Then the spinal cord was carefully separated from vertebral canal and removed along with the brain for pathological assessment of the entire central nervous system. On gross inspection, no overt inflammation or pathological changes were found in the brain or in the spinal cord regions beyond the injury site. In CTRL groups, the whole lesion area was obscured by dense, adherent scar tissue. Whereas in INCS-treated canines, scarring was markedly reduced and confined to the right lesion site, with the contralateral normal spinal cord clearly visible **(Figure 3C)**.

To evaluate whether INCS therapy promoted recovery of neurological function, we evaluated locomotor performance and muscle wasting by applying the Olby scoring system [33] and gastrocnemius muscle fiber diameter analysis **(Figure 3D)**. All groups exhibited immediate pelvic limb paralysis after hemisection, with an Olby score of zero. In CTRL group, Olby scores rapidly increased to 6.83 ± 0.95 within the 30 days post-injury (dpi), then improved gradually and plateaued at 150-180 dpi. At 180 dpi, the left pelvic limb of control canines could bear weight and showed voluntary movement, albeit with ataxic gait and frequent stumbling. The right pelvic limb retained some movement but failed to bear weight **(Figure 3E and Movie S1)**. A different pattern was observed after INCS implantation. The canines treated with INCS achieved a significantly higher score of 9.67 ± 0.33 at 30 dpi, indicating that INCS could promote

neurological recovery after SCI and potential preservation of residual contralateral spinal cord tissue. Olby scores in INCS group rose steadily, reaching a peak of 12.67 ± 0.21 at 150 dpi. At the end of the observation period, the canines in INCS group displayed weight bearing in bilateral pelvic limb, flexible walking, and coordinated gait **(Figure 3E and Movie S1)**.

SCI causes hindlimb paralysis and progressive skeletal muscle wasting, which can be determined by analyzing the pathological features and mean diameter of muscle fibers [34]. At 180 dpi, cross-sections of bilateral gastrocnemius muscles were analyzed by hematoxylin and eosin (H&E) histology to characterize muscle fibers morphology at the cellular level. Feret diameter was measured for all muscle fibers and compared between different groups. INCS-treated canines exhibited a larger mean fiber diameter than untreated canines **(Figure 3F)**. Consistently, fiber-size distribution in the INCS group shifted toward larger diameters (45-50 μm), whereas fibers in the CTRL group were predominantly distributed in 35-45 μm **(Figure 3F)**. To normalize for individual variation, the fiber diameter of the injured gastrocnemius was divided by that of the corresponding contralateral muscle. Normalized values ranged from 0.87 to 0.91 in injured canines and, surprisingly, from 0.95 to 0.99 in canines treated with INCS **(Figure 3G)**. Cytopathological assessment showed the emergence of hyperchromatic and angular muscle fibers in the injured muscles of the CTRL group, without signs of inflammatory infiltrate or sarcolemma rupture **(Figure 3H)**. In contrast, INCS group exhibited fibers with an absence of these features. These data demonstrated that INCS promoted neurological function recovery and attenuated muscle atrophy, with muscle fiber size on the injured side approaching the contralateral side.

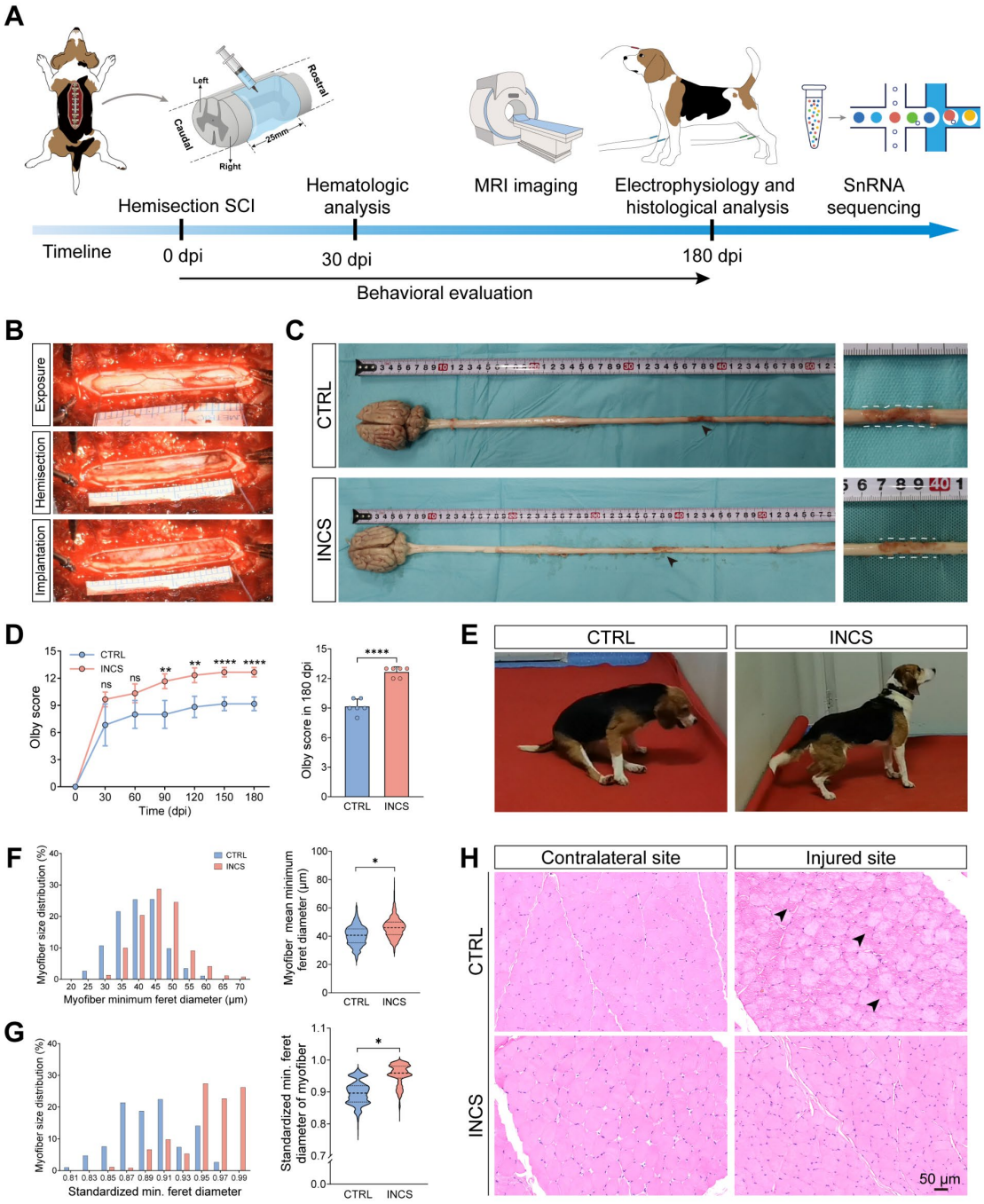


Figure 3. INCS implantation promoted motor function recovery and attenuated denervation-associated muscle atrophy after canine SCI. (A) A graphical outline showing the experimental design and analysis. (B) A long-distance spinal cord hemisection model was established, and INCS was injected into the injured region. (C) At 180 dpi after surgery, the whole spinal cord together with brain was dissected. The lesion site is indicated by the arrow. Gross pathological inspection showed that the severe adhesion and scarring were observed after SCI, but these changes were markedly attenuated following INCS implantation. (D) Olby score curves of canines in the INCS and CTRL groups throughout the observation period. (n = 6 per group; ns indicates no significance, $^{**}P < 0.01$, and $^{****}P < 0.0001$). (E) Representative images of hindlimb locomotion in beagles at 180 dpi after INCS implantation. (F) Differences in gastrocnemius myofiber size between INCS and CTRL canines are demonstrated by relative frequency histogram of the minimum feret diameter and

statistical analysis of the mean minimum feret diameter (n = 6 per group, *$P < 0.05$). (G) Normalized relative frequency histogram and mean value of myofiber minimum feret diameter, referenced to the contralateral uninjured gastrocnemius muscle of the same canine (n = 6 per group, *$P < 0.05$). (H) H&E histology images of the gastrocnemius muscle on the injured and contralateral uninjured sides in the INCS and CTRL groups. Atrophic muscle fibers are labeled by black arrows (Scale bar = 50 μm). Comparisons between two groups were performed with an unpaired t-test, and data were shown as the mean ± SEM. Longitudinal Olby scores were analyzed by two-way repeated-measures ANOVA followed by Šidák's multiple-comparison test.

INCS restored neural pathway conduction and improved bladder function after SCI

Body weight was monitored longitudinally after surgery. Regardless of INCS treatment, body weight progressively declined after SCI, reached a minimum at 30 dpi and steadily increased until completion of the observation period **(Figure 4A)**. Body weights of the INCS and CTRL groups were comparable at each time point, with no substantial difference detected. It indicated INCS implantation did not interfere with animal weight after SCI, suggesting the good biocompatibility.

Reconnection of interrupted neural pathways after SCI remains a major priority of current research. Multiple strategies have enabled neural circuit reconstruction in rodents of contusion and crush injury [35-38]. However, whether axon regeneration and function recovery can be achieved under conditions of long-distance injury is still unclear. To address this issue, cortical motor evoked potentials (CMEPs) were employed to evaluate the conduction of neural electrical signals from the motor cortex across the injury site to the effector muscle following SCI.

Electrophysiological testing was performed at 180 dpi in the hindlimb gastrocnemius muscle, with the forelimb deltoid used as an internal reference **(Figure 4B)**. CMEPs recordings in the CTRL group showed low-amplitude action potentials **(Figure 4C)**, indicating limited transmission of descending cortical signals to the hindlimb, consistent with the uncoordinated gait observed in canines **(Figure 3E)**. In contrast, INCS treatment markedly increased CMEPs amplitude, generating marked action potentials with high-peak that clearly exceeded those seen in the CTRL group **(Figure 4C and D)**, demonstrating that INCS implantation promoted reconnection of neural conduction. To account for individual variability, the amplitude recorded in the injury-side hindlimb gastrocnemius was divided by that of the ipsilateral forelimb deltoid from the same animal. The normalized action potentials showed the same trend, with the INCS group still exhibiting a markedly higher amplitude than the CTRL group **(Figure 4E)**.

As a magnetic resonance imaging (MRI) method, diffusion tensor imaging (DTI)

noninvasively reveals tissue microstructure *in vivo* through the detection of water molecule diffusion [39]. DTI is widely used to assess nerve fiber orientation in the brain and spinal cord, as water diffusion within nerve fibers is restricted by the myelin sheath barrier, creating direction-dependent displacement known as diffusion anisotropy. This property can be quantified by fractional anisotropy (FA), which allows three-dimension visualization of fiber tracts [40]. As a noninvasive imaging modality, DTI has been applied to track nerve fiber regeneration after SCI and objectively evaluate spinal cord microstructural recovery [41]. Regions at the lesion site and 12 mm rostral and caudal to the lesion were scanned to evaluate changes in the structural organization of spinal cord conducting fibers within and adjacent to the lesion **(Figure 4F)**. In uninjured spinal cord, MRI imaging showed intact spinal cord morphology, while DTI reconstruction imaging revealed continuous and well-organized blue fiber signals **(Figure 4G)**. At 180 dpi after right spinal cord hemisection, the lesion site in CTRL group exhibited a hyperintense signal on T2-weighted images, accompanied by irregular residual tissue edges, suggesting persistent edema and inflammatory changes. Correspondingly, DTI showed interruption of the organized blue fiber tracts, leaving a clear gap at the lesion center **(Figure 4H)**. In contrast, the INCS group showed no obvious T2 hyperintensity, and the remaining spinal cord tissue appeared more preserved and compact. DTI demonstrated that a considerable number of fibers crossed the lesion and reestablished the organized connection across the rostral and caudal ends **(Figure 4I)**. Anisotropy was then quantified by determining the FA values within the lesion site and in the adjacent spinal cord tissue on the rostral and caudal sides **(Figure 4J)**. Relative to uninjured canines, FA quantification showed that lesion-site values were reduced in both groups, but the INCS group exhibited greater values than the CTRL group. Rostral and caudal FA values were lower in both groups than in uninjured canines, without substantial distinction between either group **(Figure 4K)**. These findings imply that by filling the post injury tissue defect, INCS relieves edema in the spared spinal cord and facilitates the regeneration of transected nerve fibers.

SCI causes bladder areflexia and urethral sphincter dyssynergia, leading to voiding dysfunction, urinary retention, and bladder distension [42]. Histological appearance indicated that INCS treatment effectively alleviated pathological damage to the bladder. Immunofluorescence presented thickened contractile smooth layer muscle and reduced bladder volume in canines treated with INCS compared with CTRL **(Figure 4L and M)**. To assess bladder function recovery following SCI, manual bladder expression was performed to measure residual urine volume. During the first 30 dpi, residual urine volumes were comparable between the CTRL and INCS groups. Beginning at approximately 45 dpi, residual urine volume had decreased substantially in the INCS group and reached a plateau by 90 dpi. In contrast, the CTRL group exhibited a more

gradual decline, with residual urine volumes remaining relatively stable after 105 dpi. Notably, the INCS group exhibited significantly lower residual urine volumes than CTRL group at most assessed points **(Figure 4N)**. Collectively, the changes suggest that INCS facilitated reconstruction of the bladder reflex pathway after SCI, thereby indirectly protecting tissue function from secondary injury and contributing to an improved quality of life. In summary, we demonstrate that the INCS serves as a supportive matrix that allows electroneurographic signal conduction and axonal fascicle extension, providing a structural basis for the recovery of motor and bladder function.

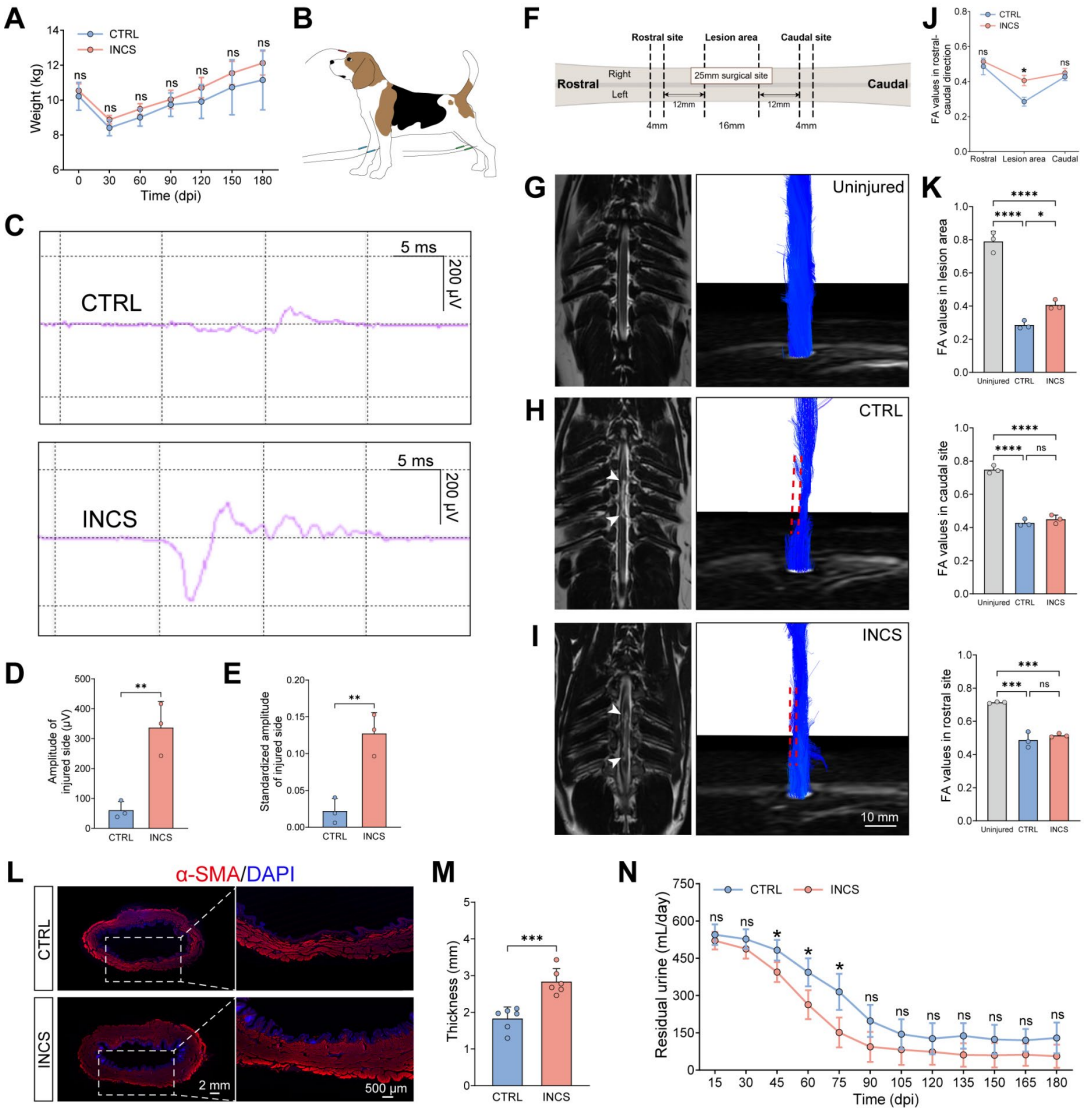


Figure 4. INCS supported neural conduction and improved bladder function. (A) Body weight changes in canines at indicated time points after treatment. (n = 6 per group, ns indicates no statistically significant difference). (B) Schematic illustration of electrophysiological testing in canines. (C) Electrical stimulation of the canine cerebral cortex recorded representative MEPs traces in right gastrocnemius. (D-E) Quantitative analysis of CMEPs amplitudes in the INCS and CTRL groups (n = 3 per group, $^{**}P < 0.01$). (F) Diagram illustrating the sites of FA measurement at different spinal cord levels. Within the 25 mm injured zone, FA values were measured in a central

16 mm core, together with the adjacent rostral and caudal segments (4 mm each). Representative coronal T2-weighted MRI images and fiber tract reconstruction of the spinal cord in uninjured canines (G), hemisected canines (H), and hemisected canines treated with INCS (I) at 180 dpi. Arrowheads in white mark the rostral and caudal margins of the lesion site, while the area enclosed by red dashed lines corresponds to the lesion site. Scale bar = 10 mm. (J-K) Line graph and bar chart depicting the differences in mean FA values at the lesion, rostral, and caudal sites between CTRL and INCS groups (n = 3 per group, ns indicates no significance, $*P < 0.05$, $***P < 0.001$, and $****P < 0.0001$). (L-M) Immunofluorescence images of the bladder wall stained for the contractile SMC marker α-SMA (red) and DAPI (blue), with quantitative analysis of bladder muscle thickness across different groups (n = 6 per group, $***P < 0.001$, scale bar = 2 mm, zoomed-in views scale bar = 500 μm). (N) Line graph showing residual urine volume measured at two-week intervals. (n = 6 per group, ns indicates no significance, $*P < 0.05$). Comparisons between two groups were performed with an unpaired t-test, while differences across several groups were assessed by one-way ANOVA followed by Tukey's test. Longitudinal data were analyzed by two-way repeated-measures ANOVA followed by Šidák's multiple-comparison test. Data were shown as the mean ± SEM.

Evaluation of the safety and biocompatibility of INCS after implantation in a canine SCI model

Foreign body response (FBR) is one of the most common immune reactions to implanted biomaterials and represents a vital criterion for evaluating transplants safety [43]. In this study, we assessed the host response to INCS implantation through hematological tests, manifestation of the implantation site, and histological analysis of major organs to provide evidence for its clinical application. Following INCS implantation, all canines received daily dedicated care. Throughout the observation period, no wound healing problems or infectious complications were observed in any of the animals **(Table S1)**. When reaching the end of the experiment, dissection of the thoracic spinal cord showed scar formation at the surgical site, with no signs of infection, hyperplasia, or other adverse reactions around the INCS implantation site **(Figure 3C)**. At 30 and 180 dpi, peripheral venous blood was collected from each canine for routine hematological, biochemical, and immunological analyses. At 30 dpi, compared with CTRL group, no obvious hepatic or renal dysfunction and no elevation of inflammation markers were detected. No abnormal changes were observed at 180 dpi **(Figure 5A-C)**.

Staining with H&E and Masson was performed to assess effects on the spinal cord, together with the principal organs including the heart, lung, kidney, liver and spleen. In INCS-treated canines, the tissue organization of the lesion site and the surrounding spinal cord parenchyma was largely preserved, with no evident hyperplasia, inflammatory cell infiltration, apoptosis, or necrosis **(Figure 6A and Figure S2A)**. Likewise, all organs exhibited normal histology regardless of INCS implantation, with no edema, inflammation, fibrosis, or other pathological alterations **(Figure 5D and Figure S1B)**. Thus, the INCS did not induce a local FBR or systemic toxicity,

highlighting the biocompatibility and safety of the material.

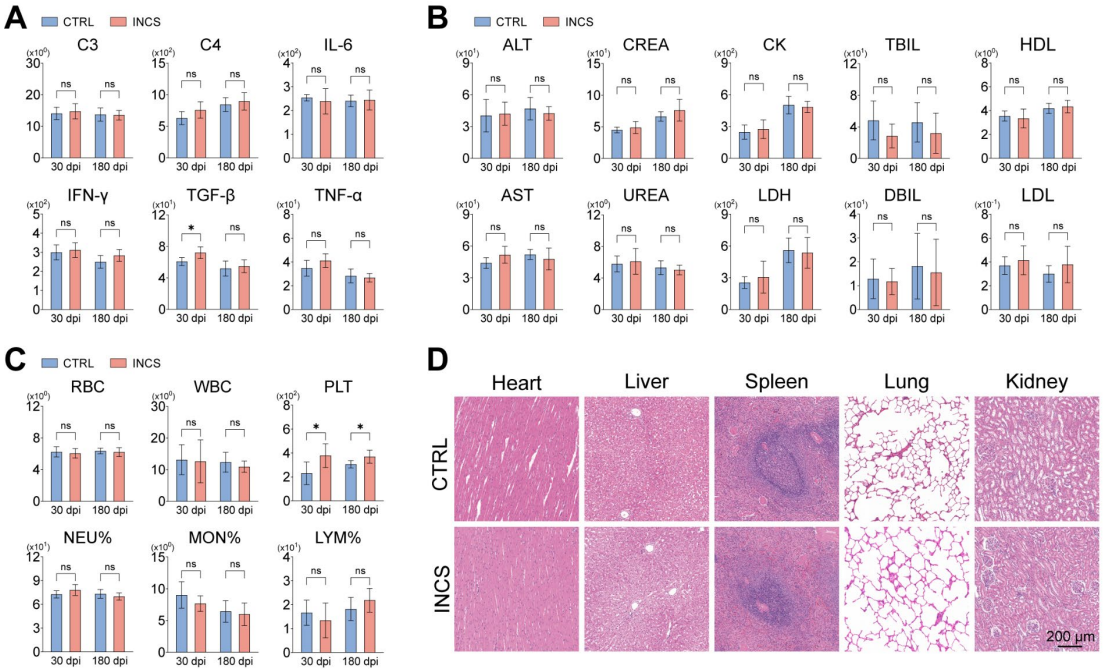


Figure 5. Biosafety evaluation of SCI dogs after INCS implantation. (A-C) Peripheral venous blood levels of C3, C4, IL-6, IFN-γ, TGF-β and TNF-α (A), and ALT, AST, CREA, UREA, CK, LDH, TBIL, DBIL, HDL and LDL (B), as well as RBC, WBC, PLT, NEU%, MON%, and LYM% in CTRL and INCS groups at 30 dpi and 180 dpi (n = 6 per group, ns indicates no significance, and $*P < 0.05$). (D) H&E staining images of the heart, lung, kidney, liver and spleen (scale bar = 200 μm). Comparisons between two groups were performed with an unpaired t-test, and data were shown as the mean ± SEM.

INCS regulated the inflammatory response and ECM remodeling in lesion sites

Following SCI, the ECM architecture at lesion site is profoundly altered, leading to extensive fibrotic scar and glial scar. Although these scar structures restrict inflammatory spread and preserve tissue integrity, they also present a major barrier to axon regeneration [44, 45]. Meanwhile, activated microglia and blood-derived monocytes that cross the blood-spinal cord barrier and differentiate into macrophages at the lesion serve to clear axonal fragments and cellular debris [46]. However, the immune cells also secrete inflammatory cytokines that amplify secondary injury through downstream cascades [47]. These cellular dynamic and matrix changes establish a complicated post-injury ECM microenvironment.

Long-segment hemisection led to atrophy of the spare spinal cord tissue and created a conspicuous tissue defect at the lesion site, which was subsequently covered by scar tissues **(Figure 6A)**. The difference was that INCS treatment maintained spinal cord integrity without appreciable collapse, and the lesion site was filled with remodeled ECM that seamlessly merged with the surrounding host tissue **(Figure 6A)**. Staining

with Masson's trichrome revealed extensive deposition of densely blue-stained collagen bundles at injured lesion in CTRL group, characteristic of fibrotic scars. Collagen fibers were also present in the INCS group, but the blue staining was markedly weaker. More importantly, red-stained matrix components were interspersed among the collagen fibers, suggesting that the matrix rebuilt by INCS converted the compact scar structure and supported the regeneration of neural tissue elements within the injured region **(Figure S2A)**. We next examined glial scar formation by immunofluorescence staining for chondroitin sulfate proteoglycans (CSPG). CSPG accumulated extensively after SCI in CTRL group, forming a dense glial scar around the damaged cord and outlining a clear graft-host boundary **(Figure 6B)**. INCS injection significantly reduced both the area and the level of CSPG staining in the lesion site **(Figure 6B and E)**.

Traumatic SCI destroys the blood-spinal cord barrier and severs supplying arteries, exposing the lesion to severe ischemia and hypoxia. Efforts to restore local perfusion have largely concentrated on promoting endothelial cell proliferation and migration [48]. However, nascent vessels often lack adequate pericyte coverage and exhibit incomplete endothelial tight junctions, which may permit leakage of inflammatory and neurotoxic mediators and thereby aggravate secondary injury. We assessed vascular regeneration using the vascular pericyte marker PDGFRβ. After long-distance hemisection, little to no vascular formation appeared in the injured spinal cord **(Figure 6C)**. By contrast, INCS treatment induced the emergence of $PDGFR\beta^+$ lumen-like structures within the lesion site, demonstrating neovascular regeneration compatible with the remodeled ECM **(Figure 6C and F)**. The perivascular localization of PDGFRβ confirms that these nascent vessels had acquired a mature phenotype and partly reconstituted the blood-spinal cord barrier. Furthermore, $PDGFR\beta^+$ cells display marked heterogeneity during tissue repair. On the one hand $PDGFR\beta^+$ cells mediate ECM remodeling and support the restoration of function after ischemic damage to neural tissue, on the other hand they are also implicated in fibrotic scarring [49, 50]. In this study, we observed that $PDGFR\beta^+$ cells accumulated in the lesion site after SCI, where they assembled into a dense network. With INCS treatment, $PDGFR\beta^+$ cells were less densely distributed and instead localized around nascent blood vessels, with greater incorporation into the ECM **(Figure 6C)**. These findings suggest that INCS redirects $PDGFR\beta^+$ cells dynamics toward ECM remodeling and neurovascular reorganization, thereby establishing a microenvironment favorable for motor and sensory recovery.

Inflammation following SCI evolves into a chronic state that can last months to years, driven by the interplay of resident microglia and infiltrated macrophages within a dynamically changing microenvironment, whose spatiotemporal evolution critically shapes neuron survival and axon regeneration [51]. However, the underlying regulatory cues are still largely undefined. We examined the inflammatory landscape after

treatment with INCS. At 180 dpi, large numbers of $CD68^+$ macrophages were still detected around the lesion, including the rostral side, the lesion core, and the caudal side, indicating that the inflammatory response had not resolved in CTRL group **(Figure 6D)**. This pattern was largely absent after INCS injection. $CD68^+$ cells were barely detectable in the lesion core, the contralateral residual tissue, or even in neighboring non-injured segments, suggesting that INCS substantially attenuated the chronic inflammatory response. Quantification of $CD68^+$ cells at corresponding lesion sites revealed a significant decrease in INCS group relative to CTRL group **(Figure 6D and G)**. The change in IBA-1^+ cells was not parallel to $CD68^+$ macrophages. We quantified IBA-1^+ cells in the lesion core, contralateral spared tissue, rostral lesion border, and caudal lesion border to assess the global immune reaction. Studies have shown that microglia depletion after SCI aggravates immune infiltration and causes neuron apoptosis, whereas locally promoting microglia proliferation contributes to neuroprotection and functional recovery [52]. INCS treatment led to a slight increase in IBA-1^+ cells in lesion epicenter and contralateral regions except the rostral and caudal lesion border, compared to untreated canines **(Figure S3A-F)**. To characterize the polarization states of microglia, iNOS and Arg1 were used as marker of pro-inflammatory (M1-like) and anti-inflammatory (M2-like) phenotypes, respectively. The results revealed that INCS implantation altered microglial polarization at the lesion site. Compared with the CTRL group, the proportion of $iNOS^+$Iba-1^+ microglia was decreased in the INCS group **(Figure 6H and I)**, whereas the proportion of $Arg1^+$Iba-1^+ microglia, which are associated with anti-inflammatory response and tissue repair, was increased **(Figure 6J and K)**. The findings suggest that INCS implantation promotes a shift in microglial polarization from pro-inflammatory toward a reparative phenotype, potentially contributing to a more favorable immune microenvironment for neuronal regeneration and tissue repair after SCI.

Overall, INCS was demonstrated to attenuate glial and fibrotic scar after SCI, ameliorate chronic inflammation, facilitate local blood vessels and ECM remodeling, and display a potent ability to enable axon regeneration.

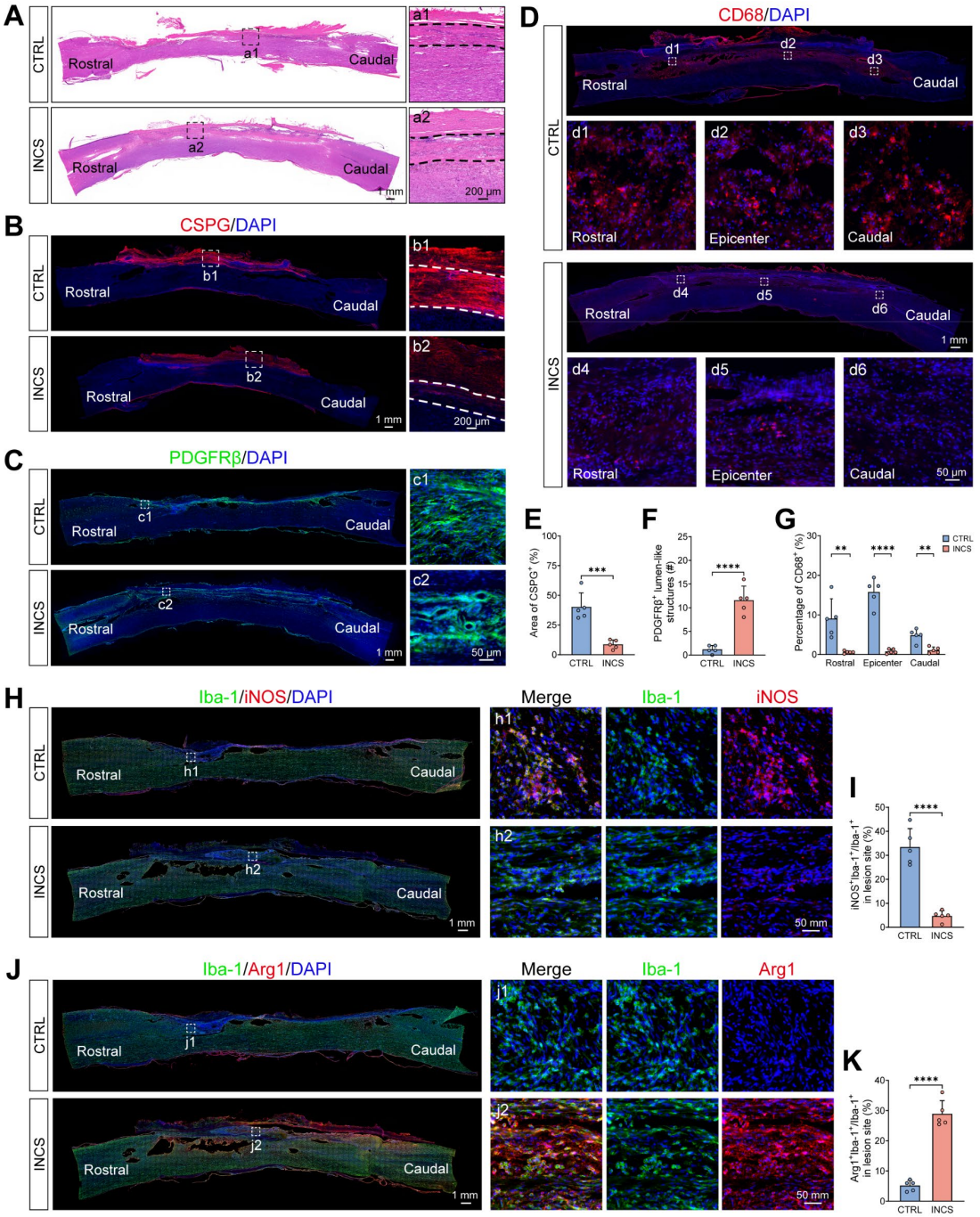


Figure 6. INCS regulated the microenvironment after SCI. (A) H&E staining reveals pathological changes at the spinal cord lesion epicenter in CTRL and INCS groups. Black dashed lines in the magnified images outline the borders of the lesion area (scale bar = 1 mm, zoomed-in views scale bar = 200 μm). (B) Immunofluorescence images of the glial scar marker CSPG at 180 dpi. INCS treatment markedly reduced both the stained area and intensity of CSPG in the lesion area. The boundary of the lesion site was delineated with white dashed lines (scale bar = 1 mm, zoomed-in views scale bar = 200 μm). (C) Immunofluorescence images of PDGFRβ$^+$ lumen-like structures in the lesion site of the CTRL and INCS groups (scale bar = 1 mm, zoomed-in views scale bar = 50 μm). (D) Images of CD68 immunoreactivity in the spinal cord lesion area of the CTRL and INCS groups at 180 dpi. Enlarged images of the rostral side, epicenter, and caudal side in lesion area are presented (scale bar = 1 mm, zoomed-in views scale bar = 50 μm). (E) The bar charts show

statistically significant differences in the CSPG$^+$ areas between the CTRL and INCS groups. (F) Quantitative analysis of the PDGFRβ$^+$ lumen-like structures number in the lesion site. (G) The proportions of CD68$^+$ cells in the rostral, epicenter, and caudal regions of the lesion area differed significantly between the CTRL and INCS groups. (H) Immunofluorescence images showing Iba-1 (green) and iNOS (red) staining of the spinal cord lesion in the CTRL and INCS group (scale bar = 1 mm, zoomed-in views scale bar = 50 μm). (I) Quantitative analysis of the percentage of iNOS$^+$ microglia in the spinal cord lesion site. (J) Immunofluorescence images of Iba-1 (green) and Arg1 (red) staining in the spinal cord lesion of the INCS and CTRL groups (scale bar = 1 mm, zoomed-in views scale bar = 50 μm). (K) Quantitative assessment of the percentage of Arg1$^+$ microglia within the spinal cord lesion site. n = 5 per group, $^{**}P < 0.01$, $^{***}P < 0.001$, $^{****}P < 0.0001$. Comparisons between two groups were performed with an unpaired t-test, and data were shown as the mean ± SEM.

INCS facilitated long-distance axon regeneration in the lesion site after SCI

Axon regeneration in adult mammals after SCI is severely constrained by both poor intrinsic neuron growth capacity and extrinsic barriers such as glial scar formation, myelin associated inhibitors, and chronic inflammation [53]. Therefore, promoting long-distance axon regeneration across the lesion remains a major unmet challenge. Here, we demonstrate that transplantation of INCS effectively overcomes the limitation, enabling robust long-distance axon regeneration across a 25 mm gap in canine model of hemisection injury.

We examined axon regeneration in the lesion site using Tuj-1 staining. In the absence of treatment, the lesion core was largely devoid of Tuj-1$^+$ signal, with only occasional Tuj-1$^+$ fibers and no morphological evidence of axons bridging the defect **(Figure S4A)**. But INCS-treated canines exhibited abundant Tuj-1$^+$ staining throughout the lesion core **(Figure 7A, Figure S4B)**. The Tuj-1$^+$ fibers were arranged in parallel to the rostro-caudal axis and extended across the full length of the lesion, reaching from the rostral to the caudal host-graft boundary, indicating strong axon regrowth and elongation in the presence of INCS. Quantification further confirmed that more Tuj-1$^+$ axons were present inside the lesion in INCS group versus CTRL group **(Figure 7D, Figure S4C-E)**. NF200 is a cytoskeletal protein expressed in neuron axons and widely serves as a relatively specific marker of mature axon fibers. It was then used to test whether the regenerated fibers had reached a mature state. In the CTRL group, canines showed negligible NF200$^+$ staining in the lesion site **(Figure S5A)**. By contrast, in the INCS group, NF200$^+$ fibers were clearly detected within the resected gap and extended discontinuously from the rostral toward the caudal stump **(Figure 7B, Figure S5B)**. The spatial distribution of NF200$^+$ fibers was broadly similar to that of Tuj-1$^+$ fibers, but the overall NF200$^+$ signal was less abundant. Quantitative analysis revealed that NF200$^+$ axons were substantially more numerous in INCS group compared to CTRL

group **(Figure 7E, Figure S5C-E)**. The presence of $NF200^+$ axons suggests that INCS supports axon regeneration as well as the maturation of regenerated fibers. Luxol fast blue (LFB) staining was used to assess the extent of myelin damage, demyelination, and remyelination. At 180 dpi, the lesion center within the resected spinal cord area exhibited a pronounced loss of blue staining accompanied by vacuolar changes. However, in treatment with INCS, newly formed myelin tracts were observed in the lesion core. LFB stained these tracts as parallel, blue-colored longitudinal strands that extended intermittently from the rostral to the caudal side of the lesion **(Figure 7C, Figure S2B)**. Strikingly, on the rostral side, these myelin sheaths displayed scattered spaced gaps, which meant formation of the nodes of Ranvier. Quantitative analysis showed that the INCS group contained significantly more myelinated profiles than the CTRL group **(Figure 7F)**. To further evaluate the myelination of axons, we examined the distribution of the voltage-gated sodium channel Nav1.6 and contactin-associated protein (Caspr), which are localized at the node of Ranvier and paranodal regions, respectively. In the INCS group, discrete and segmented $Caspr^+$ signals were observed at the lesion site, with $Nav1.6^+$ signals located between adjacent $Caspr^+$ segments **(Figure 7G and H)**. In contrast, neither signal was detected at the lesion site in the CTRL group **(Figure S2C)**. This organized nodal-paranodal distribution suggests more mature advanced myelin maturation around regenerated axons and provides structural evidence for the potential restoration of saltatory conduction. Overall, these findings indicate that INCS provides a permissive microenvironment for long-distance axon regeneration after SCI and promotes the maturation and myelination of newly regenerated axons, which are critical steps for functional recovery.

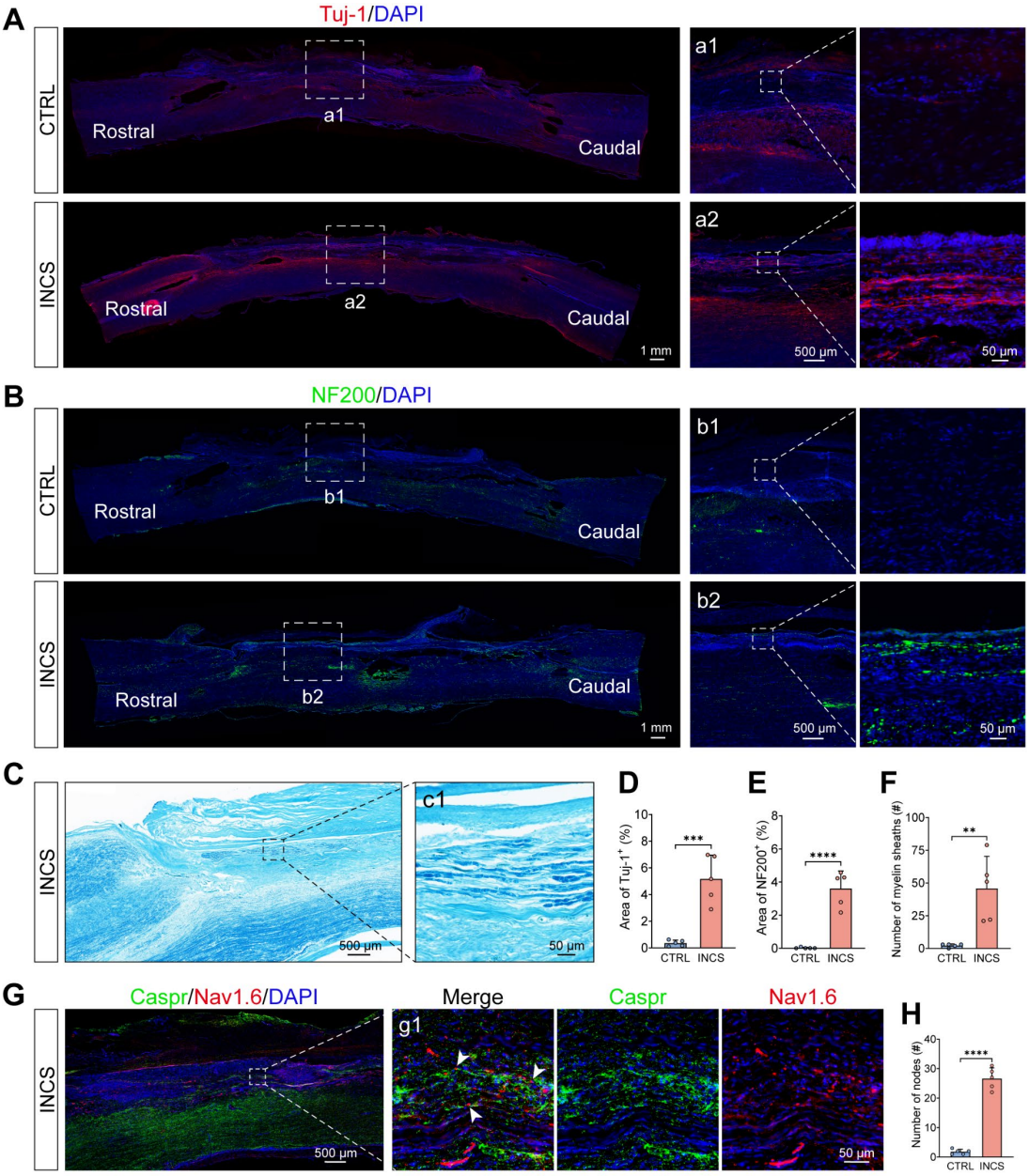


Figure 7. The INCS guided long-distance axon regeneration after SCI. (A-B) At 180 dpi after SCI, representative immunofluorescence images of Tuj-1$^+$ (A) and NF200$^+$ (B) in the lesion area of the CTRL and INCS groups, together with corresponding magnified images of typical regions (scale bar = 1 mm, zoomed-in views scale bar = 50 μm). (C) LFB staining reveals regenerated myelin sheaths extending from the rostral to the caudal side in the INCS group lesion area. Magnified views of myelin sheaths at different locations (scale bar = 500 μm, zoomed-in views scale bar = 50 μm). (D-E) Quantitative analysis of the relative fluorescence area of Tuj-1 (D) and NF200 (E) in the lesion site. (F) Quantitative analysis of myelin content in the spinal cord lesion site. (G) Nav1.6 (red) and Caspr (green) co-staining marked the nodes of Ranvier and paranodes in INCS group, respectively. Arrows indicate nodes of Ranvier (scale bar = 500 μm, zoomed-in views scale bar = 50 μm). (H) Quantitative analysis of nodal-paranodal structure numbers. n = 5 per group, $^{**}P < 0.01$, $^{***}P < 0.001$, and $^{****}P < 0.0001$. Comparisons between two groups were performed with an unpaired t-test, and data were shown as the mean ± SEM.

INCS promoted neural circuits reconstruction and ascending–descending axonal relay after SCI

Spasticity, neuropathic pain, and autonomic dysreflexia after SCI stem from lost supraspinal control together with aberrant remodeling in local cord circuits [54]. Rebuilding spinal circuitry and restoring synaptic specificity are crucial for the recovery of motor, sensory, and autonomic functions.

Calcitonin gene-related peptide (CGRP) is a neuropeptide known to mediate nociceptive transmission and has been associated with primary sensory relay and chronic neuropathic pain. After SCI, $CGRP^+$ fibers were retained at the caudal border of the lesion site **(Figure 8A)**. In contrast to the CTRL group, INCS treatment permitted $CGRP^+$ fibers to extend rostrally across the lesion site. This was evidenced by the presence of $CGRP^+$ staining within the lesion epicenter and rostral to it in the INCS group **(Figure 8A and D)**. Although only a limited number of $CGRP^+$ fibers traversed the barrier, these findings indicate that INCS creates a permissive substrate for ascending sensory projections toward the thalamus and higher centers.

5-HT release in the ventral horn plays a critical role for regulating motoneuron excitability and rhythmic activity. In CTRL canines, $5\text{-}HT^+$ staining was nearly absent from the lesion epicenter and its surrounding region. In the INCS group, however, abundant $5\text{-}HT^+$ axons projecting from the rostral spinal cord through the remodeling ECM and reaching the caudal host tissue, demonstrating long-distance bridging of the injured segment **(Figure 8B)**. Quantification showed that $5\text{-}HT^+$ fibers differed significantly between the two groups **(Figure 8E).** Notably, at the rostral and caudal graft-host boundaries, a subset of $5\text{-}HT^+$ fibers showed colocalization with $CGRP^+$ staining, raising the possibility that the regenerating axons had undergone more advanced remodeling or functional integration. Regeneration of serotonergic axons is closely associated with locomotor recovery in vertebrates, and accordingly, canines in the INCS group exhibited a more coordinated and agile gait **(Figure 3E)**.

Meanwhile, tyrosine hydroxylase (TH) positive fibers appeared in both the rostral and caudal lesion margins in the INCS group, but were scarcely seen in the CTRL group **(Figure 8C)**. TH identifies the catecholamine system, which shares the same monoaminergic descending modulatory class as 5-HT. Local remodeling of TH^+ neurons after SCI has been implicated in regulation of the micturition reflex. INCS treatment was accompanied by clear alleviation of urinary retention, with no evident bladder distension and preserved thickness of the detrusor muscle layer **(Figure 4L and M)**. These changes may be associated with local sprouting of TH^+ neurons and reconstruction of regulatory pathways at the injured borders. Quantitative analysis of the rostral and caudal injury borders confirmed a far higher density of TH^+ fibers in the

INCS group than in CTRL group **(Figure 8F)**. In general, these indicate that INCS not only enables axons to traverse the lesion and supports ascending and descending signal relay, but also integrates effectively with host tissue to foster local potential circuit reorganization associated with recovery of motor, sensory, and autonomic function.

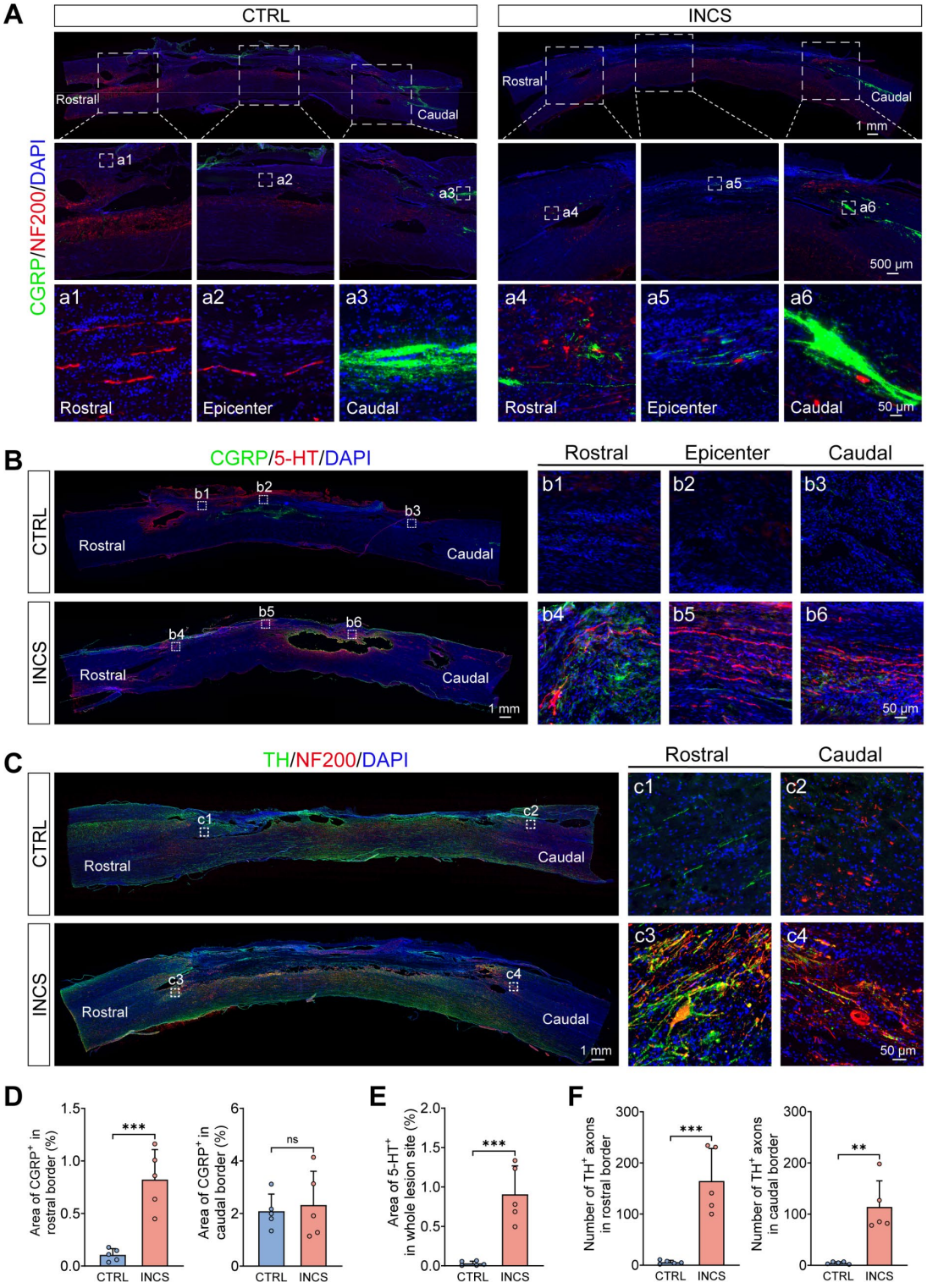


Figure 8. INCS reconstructed functional neural connection after SCI. (A) Low-magnification views of CGRP$^+$ nerve fibers, NF200$^+$ axons (red), and DAPI (blue) in the INCS and CTRL groups (scale

bar = 1 mm). Enlarged images of the rostral border, epicenter, and caudal border are also presented (scale bar = 50 μm). (B) Low-magnification views of $CGRP^+$ nerve fibers, $5\text{-}HT^+$ nerve fibers (red), and DAPI (blue) in the INCS and CTRL groups (scale bar = 1 mm). Enlarged images of the rostral border, epicenter, and caudal border are also presented (scale bar = 50 μm). (C) Low-magnification views of TH^+ nerve fibers, $NF200^+$ axons (red), and DAPI (blue) in the INCS and CTRL groups (scale bar = 1 mm). Enlarged images of the rostral and caudal border are also presented (scale bar = 50 μm). (D) Bar plot showing quantitative statistics of the CGRP positive area at rostral and caudal border in two groups. (E) Bar plot showing quantitative statistics of the $5\text{-}HT^+$ area at whole lesion site in the CTRL and INCS groups. (F) Bar plot showing quantitative statistics of the number of TH^+ axons in the CTRL and INCS groups. n = 5 per group, $*P < 0.05$, $**P < 0.01$, and $***P < 0.001$. Comparisons between two groups were performed with an unpaired t-test, and data were shown as the mean ± SEM.

INCS reshaped the cellular landscape and activates pro-regenerative neuron–microglia signaling after SCI

To profile the cellular landscape following INCS treatment after SCI, we performed single-nucleus RNA sequencing (snRNA-seq) on spinal cord tissues from the lesion core of CTRL and INCS groups at 180 dpi, respectively. After quality control filtering to exclude cells of poor quality and doublets, 41,828 cells were retained for subsequent analysis. To identify cell types, we performed unsupervised clustering on the entire dataset and manually annotated the clusters according to the expression of reference marker genes [55-59]. The coarse identified cell types included neurons, microglia, astrocytes, oligodendrocytes, Schwann cells, oligodendrocyte precursor cells (OPCs), T cells, monocytes, endothelial cells, pericytes, erythroid cells and ependymal cells **(Figure 9A)**. The top differential expressed genes (DEGs) defined a distinct molecular signature for each cell type **(Figure 9B)**. SnRNA-seq analysis showed that the uninjured spinal cord was composed predominantly of neurons and oligodendrocytes. At 180 dpi, the proportions of several cell populations changed, neurons decreased from 39.2% to 37.2%, oligodendrocytes decreased from 32.3% to 10.7%, and microglia increased from 15.3% to 29.4%. INCS treatment altered the cellular landscape after SCI. The proportion of neurons increased to 38.6%, oligodendrocytes rose to 13.4%, and microglia further increased to 31.7% **(Figure 9C and D)**. Then we asked whether the shift in cellular composition was accompanied by neurons genetic changes after INCS treatment. Analyses of DEGs detected 842 downregulated genes and 3,438 upregulated genes in samples of INCS group, with the top 20 changed genes shown in **Figure 9E** and **Figure S6A**. We observed that INCS implantation upregulated *Tktl1* expression, a gene from the same family as Tkt. Recent study has proved that activation of the pentose phosphate pathway (PPP) after SCI drives metabolic reprogramming and facilitates motor axon growth as well as sensory recovery [60]. Specifically, overexpression of Tkt or oral D-ribose can activate the PPP and promote neurological

improvement. As *Tktl1* is a member of the transketolase family, the data suggests that INCS may engage the PPP through *Tktl1* upregulation, which could contribute to long-distance axonal regrowth and improved function after SCI. Gene ontology (GO) analysis showed that genes upregulated in neurons of INCS group were associated with cell adhesion, signal transduction, glutamatergic synapse, dendritic spine, presynaptic membrane **(Figure S6B)**. Kyoto Encyclopedia of Genes and Genomes (KEGG) enrichment analysis also revealed that the upregulated pathways in neurons of INCS group were cell adhesion molecules, glycosaminoglycan biosynthesis, and rap1 signaling pathway, while downregulated pathways included hippo signaling pathway, IL-17 signaling pathway, and ferroptosis **(Figure S6C)**. These findings suggest that migration, regeneration, and synapse formation related genes were activated in neurons following INCS treatment, thereby facilitating the repair and regeneration of damaged tissues. In addition, GO analysis of microglia showed that microglia in INCS group were highly enriched in biological processes and cellular components related to glutamatergic synapse, axons, and synapse assembly (**Figure 9F**), suggesting that microglia may create a permissive milieu for neuron regeneration.

To understand cell-cell communication in the injured microenvironment, we systematically screened ligand-receptor pairs across the annotated cell types. Compared with CTRL group, the INCS group exhibited both more numerous interactions and more robust interaction strength **(Figure S6D and E)**. Among identified signaling pathways, Spp1 and Fn1 were markedly upregulated after INCS treatment **(Figure 9G)**. Analysis of pathway-specific communication networks further showed that interactions mediated by Spp1 and Fn1 pathways were notably increased across multiple cell types, particularly in neurons **(Figure 9G and Figure S6F and G)**. Previous studies have shown that microglia with $Spp1^{+}$, $Ms4a7^{+}$, and $Fn1^{+}$ signatures promote scar-free healing after SCI [61]. In our analysis, neuron-microglia interactions were concurrently increased in both the Spp1 and Fn1 pathways in INCS group. Given the concomitant reduction in scarring and promotion of axon regeneration after INCS treatment, these findings point to a key role for microglia in the repair process.

INCS promoted reparative microglial programs supporting axon extension, ECM remodeling, and circuit plasticity

The heterogeneity of microglia exerts profound control over the immune microenvironment and regenerative trajectory after SCI [62]. We therefore performed further clustering analysis on microglia and identified seven distinct subtypes **(Figure 9I and J)**. Based on characteristic markers and DEGs analysis, we annotated these cells as homeostatic microglia, $Fmn1^{+}$ microglia, inflammatory microglia, disease associated microglia like microglia (DAMLM), $Spp1^{+}$ microglia, proliferated microglia, and lipid

droplets-accumulating microglia (LDAM). The microglia landscape altered markedly after injury, with a significant reduction in homeostatic microglia and expansion of DAMLM and inflammatory microglia. INCS treatment partially reversed this pattern, increasing the proportions of homeostatic, $Fmn1^+$, and $Spp1^+$ microglia while reducing inflammatory microglia, LDAM, and DAMLM. Notably, $Fmn1^+$ microglia expanded from 17.60% to 29.88% and became the dominant subtype in INCS group **(Figure 9K)**. The change indicates that INCS suppresses microglial states that are detrimental to repair.

High proportion of $Fmn1^+$ microglia prompted us to explore their functional feature. Characteristic expression mark genes of $Fmn1^+$ microglia contained *Rph3a*, *Hs3st3a1*, *Igf2bp2*, *Slc26a8*, *Ssx2ip*, and *Nyap2*. These top signature genes mainly participate in dendritic spine formation, organ development, proliferation, and cell migration **(Figure S7A)**. GO analysis showed that $Fmn1^+$ microglia expressed molecular function terms related to signal transduction, cell adhesion, and semaphorin activity **(Figure 9L)**. Enriched cellular components included glutamatergic synapses, axons, synaptic vesicles, and postsynaptic membranes **(Figure 9M)**. Biological process terms were dominated by postsynaptic organization, nerve development, axon extension and guidance, and ECM organization **(Figure 9N)**. KEGG enrichment identified pathways involving ECM-receptor interaction, cell adhesion molecules, MAPK, PI3K-AKT, and citrate cycle **(Figure 9O)**. These features of $Fmn1^+$ microglia are consistent with roles in axon growth and ECM remodeling, and that unique functional state is preferentially activated after INCS implantation. Alongside $Fmn1^+$ microglia, $Spp1^+$ microglia also increased under INCS treatment. Consistent with earlier reports, $Spp1^+$ microglia were enriched in genes linked to ECM, migration, and signaling regulation **(Figure S7C-E)**, and they upregulated PI3K-AKT and axon guidance pathways **(Figure S7B)**, supporting a beneficial role in debris clearance, ECM remodeling, pro-regenerative cell–cell communication, axon guidance, and potentially remyelination after SCI [61, 63-65]. Subsequently, we further performed immunofluorescence to validate the snRNA-seq findings. The results showed that $Spp1^+$ microglia were distributed in the lesion site, with significantly greater numbers in the INCS group compared to CTRL group **(Figure 9P and R)**. Meanwhile, Iba-1/Fmn1 co-staining revealed clear co-localization of Fmn1 and Iba-1 **(Figure 9Q)**. Consistent with the transcriptomic expansion of this cluster, the proportion of $Fmn1^+$Iba-1^+ cells were markedly elevated in the INCS group relative to CTRL group. Spatially, the $Fmn1^+$Iba-1^+ cells were predominantly enriched at the lesion border. Morphologically, Fmn1 protein was not diffusely distributed throughout the cytoplasm but instead concentrated within the perinuclear region or polarized toward one side of the soma. These cells typically displayed enlarged somata with shortened processes, adopting a polarized or amoeboid

morphology **(Figure 9Q, q2)**. To determine whether the Fmn1^{+}Iba-1^{+} cells overlapped with other populations or were associated with previously described microglial states, we co-stained Fmn1 with Gpnmb, iNOS, and Spp1. Surprisingly, minimal co-localization was observed between Fmn1 and any of these markers **(Figure S7F–H)**, indicating that the Fmn1^{+} population is distinct from DAMLM, inflammatory microglia and Spp1^{+} microglia. Overall, we identified a microglia subset elicited by INCS that deviates from classical immune phenotype. Instead, it promotes axon extension, restructures ECM, organizes postsynaptic components to facilitate circuit plasticity, and supports neuron survival and axon growth through VEGF receptor and MAPK/PI3K-AKT signaling pathway. This population thus represents a promising endogenous mediator of post-injury spinal cord repair.

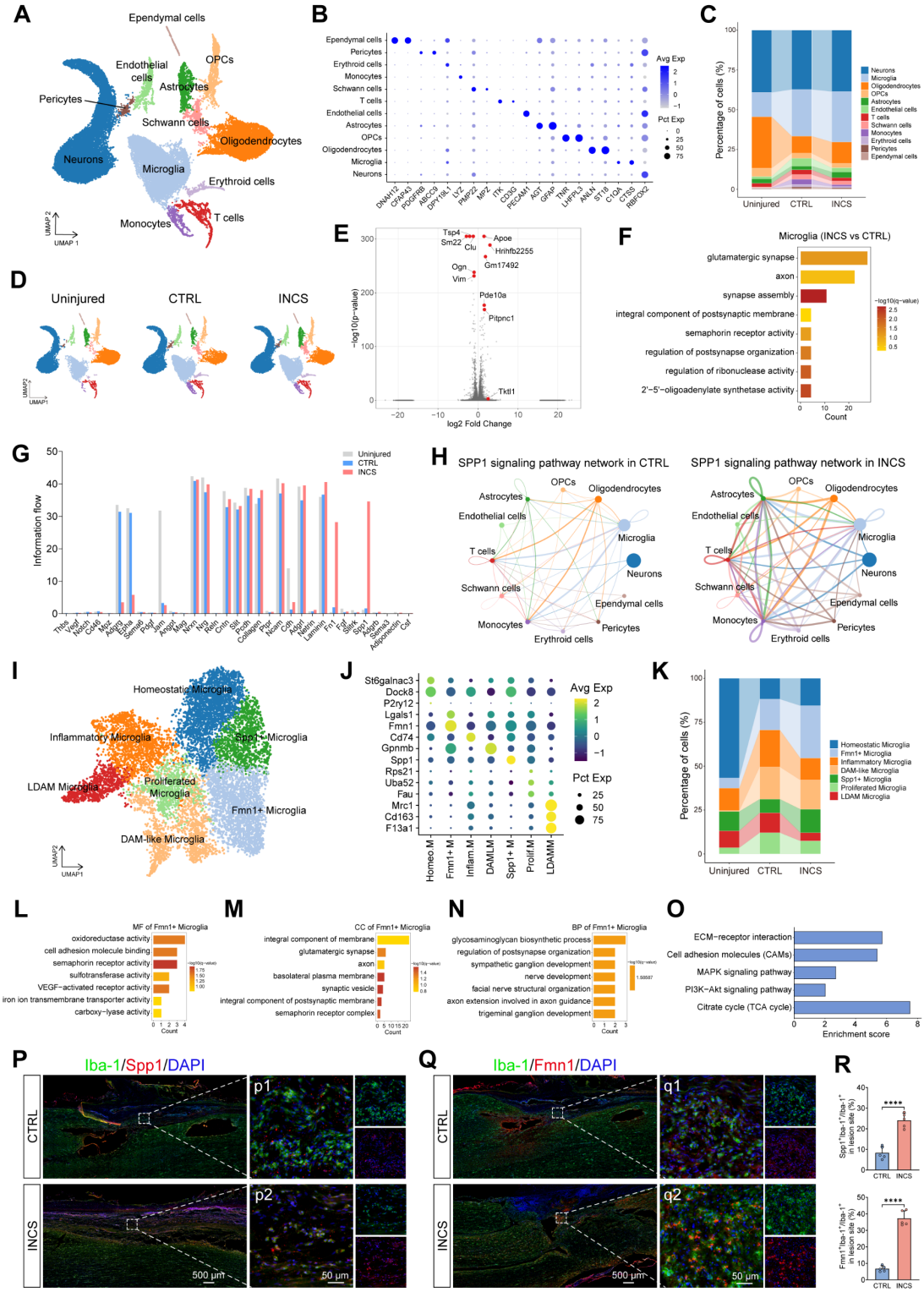


Figure 9. Single-nucleus atlas revealed the INCS reshaped the cellular landscape and activated pro-regenerative neuron–microglia signaling after SCI. (A) UMAP visualization of the 41,828 cells sequenced from the injured spinal cord identified 12 major cell types according to characteristic gene marker expression, which were color-coded accordingly. (B) Dot plot illustrating the DEGs for every major cell class. Color depth reflects the level of expression of corresponding gene, while the size of each dot shows the proportion of the cells expressing it. (C) Changes in the proportion of each cell type across uninjured, CTRL, and INCS group. (D) UMAP plots showing the cellular

composition of the spinal cord in the uninjured, CTRL, and INCS groups. (E) Volcano plot showing expression changes in neurons, comparing INCS vs CTRL groups. (F) GO enrichment analysis for microglial DEGs, comparing the INCS and CTRL groups. Adjusted *P* values were estimated using false discovery rate (FDR). (G) Bar chart comparing the signaling pathway information flow among all coarse classified cells in uninjured, CTRL, and INCS groups. (H) Interaction networks of cell-cell communication depicting the number of intercellular interactions in the Spp1 signaling pathway among different cell types in the INCS and CTRL groups. Thicker lines indicate more detected interactions between cell types. (I) UMAP visualization plot showing seven microglia clusters. (J) Dot plot showing the differentially expressed genes for each microglia subtype. (K) Changes in the proportion of each microglia subtype across uninjured, CTRL, and INCS group. (L-N) GO enrichment analysis of upregulated genes in $Fmn1^+$ microglia in terms of molecular function (L), cellular component (M), and biological process (N). Adjusted *P* values were estimated using FDR. (O) Pathway enrichment results from KEGG for upregulated DEGs in $Fmn1^+$ microglia. (P) Iba-1 (green) and Spp1 (red) co-staining in the lesion site of CTRL and INCS groups. (Q) Iba-1 (green) and Fmn1 (red) co-staining in the lesion site of CTRL and INCS groups. (R) Quantification of $Spp1^+Iba\text{-}1^+$ and $Fmn1^+Iba\text{-}1^+$ cells as a percentage of total $Iba\text{-}1^+$ microglia (n = 5 per group, scale bar = 500 μm, zoomed-in views scale bar = 50 μm). Comparisons between two groups were performed with an unpaired t-test, and data were shown as the mean ± SEM.

Discussion

Dyskinesia below the level of traumatic SCI originates largely from the limited regeneration ability of damaged axons [53]. To address this challenge, diverse approaches have been applied for SCI repair [3, 10, 66]. By preserving the biological properties and physicochemical signals of the ECM, ECM-derived materials have shown favorable therapeutic outcomes in SCI repair [18]. Nevertheless, practical limitations of ECM-derived materials include interspecies rejection, poor mechanical stability, and complex protocols, which are obtained from rat, porcine, and rabbit, with source tissues including the spinal cord, optic nerve, sciatic nerve, and skeletal muscle [15, 18, 67]. Therefore, the selection of appropriate donor sources and tissue is particularly critical for clinical application. ECM-derived materials typically fall into two categories—scaffolds and hydrogels. High stiffness of scaffolds imposes chronic friction and compression on adjacent tissues, triggering persistent inflammation. Meanwhile, the preformed shape mismatches the irregular injured cavity and leaves residual gaps upon transplantation, which leads to scar formation and hinders axonal regrowth. Hydrogel commonly involves crosslinker, which carries potential toxicity to the organism. In addition, the process of hydrogel gelation often relies on pH, osmotic pressure, and temperature, making preparation and handling cumbersome and time-consuming.

Among tissues derived from various species, bovine tissues exhibit great biosafety and histocompatibility, owing to the structural and compositional resemblance to human

tissues. Bovine-derived tissues have been translated into clinical products, including artificial heart valves, cardiovascular patches, gelatin sponges, deproteinized bovine bone matrix, meniscal scaffolds, artificial dermis, and surgical sutures. In previous studies, we successfully developed bovine tendon-derived linear-ordered collagen scaffolds (NeuroRengen Scaffold) to treat completely transected SCI and achieved promising therapeutic efficacy. NeuroRengen Scaffold can provide directional support for neuronal growth and axonal extension to promote nerve regeneration and serve as an efficient carrier suitable for drug loading and cell transplantation [32, 68-70]. Considering that incomplete SCI predominates clinically, we further developed a bovine-based INCS for repairing irregular spinal cord defects. INCS was notably easy to apply prior to treatment, only by mixing the powder with saline and letting it undisturbed for one hour. This pattern can effectively shorten the preparation time and bring significant convenience to clinical practice. In contrast, other traditional ECM materials require complex preparation procedures and a longer waiting time [18, 21, 71]. Upon reconstitution in saline, INCS undergoes self-assembly, potentially mediated by multiple self-assembly non-covalent interactions. Hydrogen bonding contributes to the structural stability of collagen and may facilitate intermolecular association during the assembly process. Concurrently, hydrophobic interactions involving non-polar amino acid residues promote the aggregation of collagen molecules in the aqueous environment. Electrostatic interactions further modulate the molecular alignment and fibrillar organization. Collectively, these combined forces enable the dispersed collagen molecules to form a fibrillar network under physiological ionic conditions.

SEM showed that INCS had an ordered porous network structure with a pore diameter of 107.34 ± 3.24 μm, which falls within the 22-200 μm range considered favorable for neural fiber ingrowth [22, 23]. This pore architecture may facilitate directional axonal extension while providing sufficient space for axonal sprouting [72]. This network also promoted migration of vascular endothelial cells and oligodendrocyte precursor cells. Therefore, it was able to accommodate the co-growth between cells and axons, creating a microenvironment that supported vascularization, myelination and nerve regrowth. The G' and G'' of INCS remained nearly constant at 981.16 ± 6.29 Pa and 181.78 ± 0.56 Pa, respectively, which matched the mechanical properties of normal spinal cord [24, 25]. This result indicated that INCS featured highly biomimetic characteristics. Overall, these results indicated that INCS supplied stable structural support for axonal regeneration and could therefore act as a desirable material for neural repair, collectively owing to its ordered porous architecture, mechanical similarity to native spinal cord and simple preparation.

We evaluated the capacity for facilitating axonal extension and functional recovery in SCI models. An important consideration in interpreting the present findings is that the

25 mm hemisection model preserves part of the contralateral spinal cord, which may contribute to spontaneous functional recovery through spared descending pathways, compensatory axonal sprouting, and neural plasticity. Indeed, voluntary movement of the left pelvic limb was observed in the CTRL group at 180 dpi, highlighting the contribution of endogenous recovery mechanisms. Nevertheless, the INCS group exhibited more favorable hindlimb motor outcomes and less pronounced gastrocnemius muscle atrophy than the CTRL group, suggesting that INCS implantation was associated with additional functional benefits beyond those observed in untreated animals. The CMEP and DTI findings provide complementary evidence of changes in neural conduction and fiber continuity but cannot independently distinguish newly regenerated axons from spared fibers or compensatory sprouting. Therefore, the observed functional improvements may reflect a combination of INCS-associated axonal regeneration on the injured side, plasticity of spared contralateral pathways, and reorganization of spinal neural circuits. The aligned porous architecture of INCS may facilitate axonal growth and organization within the lesion. However, the specific contribution of this mechanism requires further investigation. A complete transection model would provide a complementary and more stringent approach for investigating whether INCS can support axonal growth across a lesion without spared longitudinal pathways at the injury plane. However, complete transection also produces a more severe injury and a different tissue microenvironment, potentially affecting both regenerative responses and functional recovery. Future studies incorporating rigorously verified complete transection models, together with tract-specific tracing and appropriate functional assessments, will be important for determining the extent to which INCS-mediated recovery depends on de novo axonal regeneration across the lesion gap.

Excessive ECM deposition following SCI hinders neural regeneration [11]. Histological analysis revealed significant reductions in scar formation and inflammatory infiltration after INCS implantation. Together with main organ pathological analysis and hematological results, it illustrated that INCS owned favorable biocompatibility and low immunogenicity. Thus, INCS was more likely to be recognized as an autologous substance, which reduced the secretion of pro-inflammatory mediators and restrained the downstream inflammatory response. Notably, following INCS intervention, PDGFRβ$^+$ cells shifted from dense aggregates forming to promoting new vessels mature and ECM remolding, which indicated that PDGFRβ$^+$ cells contribute to blood-spinal cord barrier repair and amelioration of the injury microenvironment. Newborn neuron and neurofilament staining confirmed that INCS sustained neuronal survival and allowed axons to bridge the long-distance injury site. Moreover, INCS also facilitated axonal myelination and supported descending

electrical signal transmission to the pelvic limbs, suggesting restoration of the structural basis required for rapid electrical conduction. In parallel, CGRP/NF200 co-staining identified that ascending fibers could extend across the long-distance lesion area, confirming the presence of the structural basis for sensory signal projecting to the thalamus and other higher centers. This illustrated that INCS may build the signal conduction circuit between the supraspinal centers and the lower centers, through its topological architecture guiding the orderly alignment of descending and ascending fibers. Therefore, based on stable ordered porous architecture and biocompatibility, INCS can remodel the ECM and create a favorably regenerative microenvironment for long-distance axonal regrowth, which facilitated potential circuit reorganization and functional recovery.

Subsequently, we used snRNA-seq to explore the underlying mechanisms of long-distance axonal regeneration driven by INCS. Cell-type proportion analysis revealed that SCI substantially depleted neuronal and oligodendrocyte populations, whereas INCS treatment increased their relative abundance, consistent with our *in vivo* results. These findings showed that INCS increased the survival of neurons and oligodendrocytes, supplying the cellular basis required for axon regeneration and remyelination. It has been reported that the PPP pathway promotes nerve regeneration, with *Tkt* serving as a key protein [60]. DEGs analysis revealed that *Tktl1*, a homolog of *Tkt*, was substantially upregulated after INCS treatment. This suggested that INCS may activate the PPP through upregulation of *Tktl1*. Consequently, it may trigger downstream regenerative processes and potentially explain the enhanced neuronal survival and functional recovery observed *in vivo*. Consistent with Iba-1 immunostaining, INCS intervention also increased the proportion of microglia. Microglial subcluster analysis revealed the reduction in LDAM, DAMLM and inflammatory microglia, accompanied by an increase in homeostatic, $Fmn1^+$ and $Spp1^+$ microglia. Notably, $Spp1^+$ microglia has been reported to facilitate scar-free healing after SCI [61], which was supported by our cell-cell communication analysis. Among microglial subpopulations, $Fmn1^+$ microglia accounted for the largest proportion. GO and KEGG enrichment analyses indicated that $Fmn1^+$ microglia might induce cell migration and signal transduction through activation of the MAPK/PI3K-AKT pathway. Although snRNA-seq identified Fmn1-expressing microglial populations, increased *Tktl1* expression, and predicted Spp1/Fn1-associated ligand–receptor communication following INCS implantation, these findings primarily represent transcriptomic associations at 180 dpi. Additional immunofluorescence analyses supported the presence of Fmn1-expressing Iba-1^+ cells and an increased representation of $Spp1^+$Iba-1^+ cells in the INCS group. However, these observations do not establish that Fmn1 or Spp1 directly mediates tissue repair, nor do they demonstrate the functional activity of

the predicted ligand–receptor interactions. Similarly, the potential involvement of *Tktl1* in metabolic reprogramming remains to be experimentally established. Future studies employing targeted loss-of-function and gain-of-function approaches, together with direct validation of candidate signaling interactions and their downstream effects, will be necessary to determine whether these molecular candidates causally contribute to INCS-mediated repair.

An important limitation of this study is that histological assessments were performed only at 180 dpi, precluding longitudinal characterization of INCS degradation and early host-biomaterial interactions. At the 180 dpi, no obvious residual INCS fragments were identified in the examined lesion sections, and inflammatory cell infiltration was less pronounced in the INCS group. These findings support favorable long-term tissue remodeling without an overt persistent inflammatory response at the endpoint. However, they do not establish the rate or completeness of scaffold degradation, the timing of host tissue infiltration, or the nature and duration of the early FBR. In particular, the absence of visible residual fragments at the endpoint should not be interpreted as definitive evidence of complete material resorption. Future studies incorporating serial histological assessments at early and intermediate time points, together with quantitative evaluation of scaffold persistence, tissue infiltration, and macrophage responses, are warranted to elucidate the degradation kinetics and host response to INCS. Another one is the absence of anterograde and retrograde tract tracing, which is technically demanding in large animals and requires intracranial tracer injection, prolonged survival, and specialized histological processing. Therefore, we could not completely determine whether axons crossing the lesion originate from supraspinal centers or sprouting. Although histological and electrophysiological evidence supports axon extension and functional conduction, further tracing studies are needed to confirm the origin of axons.

In this study, we identified an unrecognized mechanism which involved the activation of Tktl1-associated PPP and enrichment of $Fmn1^{+}$ microglia. Although it remains unclear how the topographical and mechanical properties of INCS are sensed by cells, and whether distinct neuronal subtypes share a common mechanism of *Tktl1* upregulation. Both of problems require further investigation. From a perspective of clinical translation, the simplicity of INCS preparation and the ease of its application support the preclinical value and practical scalability. Future strategies could combine INCS with other biological approaches, such as stem cells, organoids and antibodies. It could also incorporate physical interventions, including electrical stimulation, magnetic fields, and infrared light, to further enhance regeneration. These approaches may provide more efficient therapies for SCI repair.

Conclusion

In summary, this study demonstrates that INCS effectively promotes long-distance axon regeneration across the injury site in a pre-clinical large animal model. INCS remodeled the injury site microenvironment by attenuating glial and fibrotic scarring, dampening chronic inflammation, and supporting ECM reorganization. Histology analysis showed increased regeneration of nascent and mature axons, accompanied by myelination. Moreover, INCS contributed to reconstruction of descending serotonergic and noradrenergic fibers, as well as ascending CGRP projections, suggesting the restoration of structural continuity for these neural tracts at the lesion site. These microstructural improvements correlated with significant recovery of motor function, electrophysiological conduction, and bladder control, without signs of immune rejection or toxicity. SnRNA-seq revealed that INCS treatment activated the PPP pathway in neurons, and identified a candidate Fmn1-expressing microglial population associated with axonal outgrowth and synaptogenesis. Importantly, INCS can be stored, prepared, and delivered with minimal effort, thereby addressing major practical limitations of current ECM-derived materials. Overall, as a clinically translatable, ready-to-use biomaterial, INCS represents a new transplantation strategy for neural regeneration and holds promise for improving functional recovery and quality of life in SCI patients.

Experimental section

Preparation of INCS

INCS was prepared from bovine collagen tissue by DB Wuderegen Biomedical Technologies Co., Ltd (Zhenjiang, China). Briefly, bovine skin-derived collagen tissue was sequentially processed by defatting and decellularized by 1% SDS, and lyophilization to generate a decellularized matrix, which was subsequently pulverized and ground into fine particles between 10 and 100 μm. These particles were sterilized by cobalt-60 (^{60}Co) gamma irradiation and stored as a dry powder at room temperature. Prior to use, 50 mg powder was suspended in 500 μL normal saline (100 mg/mL) and left to stand for 1 h to obtain INCS.

Rheological characterization

The rheological properties of the hydrogels were characterized using a rotational rheometer (DHR-2, TA Instruments, USA) equipped with a 20 mm parallel-plate geometry. The gap between the plates was set to 1000 μm, and all measurements were performed at 25 °C. Oscillatory rheological measurements, including frequency sweeps,

time sweeps, and amplitude sweeps, were conducted to evaluate the viscoelastic properties of the hydrogels. The storage modulus (G′) and loss modulus (G″) were recorded to characterize the elastic and viscous behavior of the hydrogels, respectively.

Proteomic analysis

The protein composition of the INCS was analyzed using data-independent acquisition (DIA)-based liquid chromatography–tandem mass spectrometry (LC-MS/MS). Briefly, proteins were extracted from the samples using SDT lysis buffer, and protein concentrations were determined using a BCA assay. Protein digestion was performed using the filter-aided sample preparation (FASP) method with trypsin. The resulting peptides were desalted, lyophilized, and reconstituted in 0.1% formic acid. Peptide separation and mass spectrometric analysis were performed using a Vanquish Neo liquid chromatography system coupled to an Orbitrap Astral mass spectrometer (Thermo Fisher Scientific, USA) in DIA mode. The acquired raw data were processed using DIA-NN software for protein identification and quantification against a bovine protein sequence database, with a false discovery rate (FDR) threshold of less than 1%.

Scanning electron microscopy

The powder of INCS was stirred with saline and left to stand for 1 h, after which the INCS was rapidly frozen using liquid nitrogen. The frozen INCS was fragmented using a scalpel blade, placed on a specimen holder and visualized with a scanning electron microscopy (S-3400N, Hitachi, Japan) at 500× and 1000× magnifications.

Quantitative DNA content analysis

The assay was conducted following a previous study [73]. In brief, INCS samples were dehydrated to constant weight, lysed in RIPA buffer, subjected to Proteinase K digestion, and then extracted using a DNA isolation kit (Y1217, TIANGEN). Samples were mixed at a 1:1 volume ratio with PicoGreen reagent, incubated, and read on a multi-mode microplate reader (BioTek, USA). The DNA content was then calculated against a DNA standard curve.

Animals and ethical approval of INCS for implantation

All experimental beagles (1-1.5 years, female, 10.38 ± 0.18 kg) were provided and housed by the Hunan Prima Medicine Research Center (Changsha, China). The study design followed the Guidance on the Registration Review of Animal Studies for Medical Devices issued by the National Medical Products Administration of China and Laboratory animals - General requirements for animal experiments (Chinese National

Standard number: GB/T 35823-2018). All procedures involving animal experimentation were comprehensively evaluated and conducted in accordance with the Guide for the Care and Use of Laboratory Animals from NRC, with approval by the Ethics Committee of Hunan Prima Medicine Research Center (approval number: IACUC-2024 (5) 026).

Surgical procedure and transplantation

The animals were fasted for 12 h before the operation. Atropine sulfate at a dose of 0.1 mg/kg was injected subcutaneously to suppress secretions from the bronchi and salivary glands. During the surgery, anesthesia was intramuscularly induced with tiletamine-zolazepam (10 mg/kg) and maintained using continuous intravenous propofol (0.2 mg/kg/min) along with intermittent intravenous fentanyl (0.002 mg/kg/30 min) [32]. Canines were intubated and equipped with an electrocardiograph monitor (MEC-1000, Mindray, China) to establish a respiratory circuit. All surgeries were performed by the same experienced neurosurgeon following a standardized protocol. After shaving fur of the back, a 10cm longitudinal incision was made over the skin of thoracic vertebral region. Fascias, muscles and adipose tissue were incised to expose the T8-T9 laminae. Following laminectomy and hemostasis with gelatin sponges, the dura mater was incised along the spinal midline. Under microscopic (TIVATO700, Zeiss, Germany) guidance, the posterior median sulcus and the posterolateral sulcus were identified as anatomical landmarks. We then made a longitudinal incision along the midline and excised a 25 mm spinal cord segment tissue from the right side. In the INCS group, the syringe tip was positioned at the rostral boundary of the lesion site, and INCS was injected slowly while the syringe was moved caudally, until the defect was completely filled. Care was taken to avoid overfilling. Whereas the CTRL group received no treatment. We also included one uninjured canine (n = 1) that underwent T8-T9 laminectomy only, without SCI or INCS implantation, and used it for subsequent snRNA-seq. After the suture of dura, muscles and skin layer in sequence, the incision was disinfected with iodine solution. The animals were covered with a blanket and kept warm until regaining consciousness.

Ceftriaxone sodium (50 mg/kg) was administered subcutaneously to all animals daily for 3 days. The incision was cleaned and disinfected daily until suture removal to promote healing, and a soft mat was provided to prevent contusion. The abdomen was manually massaged each day to assist urination and defecation until voluntary recovery of these functions was restored. After the postoperative care, canines were allowed to move freely in an open area to enhance pelvic limb recovery for 30 min each day. The weight was measured monthly, and video recordings were used for the recovery of pelvic limb locomotor function. The beagles were housed in an appropriate temperature

environment under a 12 h light-dark cycle and were given sufficient water and food.

Hematological examination

At 1 and 6 months post-surgery, whole blood was collected into serum separator tubes and EDTA anticoagulant tubes. Hematological parameters containing red blood cells (RBC), white blood cells (WBC), platelets (PLT), neutrophil percentage (Neu%), monocyte percentage (Mon%), and Lymphocyte percentage (Lym%) were measured by a hematology analyzer (BC-5000vet, Mindray).

Biochemistry and ELISA assay

Blood was drawn into serum separator tubes and spun at 3000 rpm for 15 min to collect serum for biochemical test, whose indicators included alanine aminotransferase (ALT), creatinine (CREA), aspartate aminotransferase (AST), urea (UREA), creatine kinase (CK), lactic dehydrogenase (LDH), total bilirubin (TBIL), direct bilirubin (DBIL), high-density lipoprotein (HDL), and low-density lipoprotein (LDL), were analyzed with a biochemical analyzer (Chemray 800, Rayto). For the ELISA quantification, the ELISA kits (ZciBio, China) were applied in accordance with the manufacturer's instructions. A microplate reader (RT-6100, Rayto) was used for recording absorbance and translating optical density values into concentrations. The determined indicators of ELISA were component 3 (C3), component 4 (C4), interleukin-6 (IL-6), interferon-γ (IFN-γ), transforming growth factor-β (TGF-β) and tumor necrosis factor-α (TNF-α).

Behavioral assessment

To assess pelvic limb motor recovery, the Olby score was employed in the SCI canine models [74]. Functional assessment was performed in an open field based on pelvic limb joint movement, gait coordination, deep pain sensation, weight-bearing, and voluntary tail movement. Two independent investigators blind to the group assignments determined the scores. Every animal was placed alone in an open-field arena and observed for 5 min. The Olby score spans 0 to 14, where each value reflects a defined level of pelvic limb motor function.

Bladder function assessment

Following SCI, bladder dysfunction is reflected by an inability to fully empty the bladder. The volume of residual urine is used as a quantitative measure for assessing bladder dysfunction. To evaluate urinary retention, we manually expressed the bladders twice a day and recorded the urine volume each time. Daily total urine volume was calculated by summing the two values (mL/day).

Electrophysiology

Following the induction of anesthesia with tiletamine-zolazepam (10 mg/kg), electrophysiological testing was assessed the integrity of nerve conduction. CMEPs was recorded using an electrophysiological testing device (Xltex-protektor 16-channel type, Xltex, Canada) with stimulating electrodes positioned at designated sites. In brief, Transcranial electrical stimulation was delivered over the precentral gyrus. Recording electrodes were placed in the deltoid (forelimb) and gastrocnemius (hindlimb). Forelimb MEPs recorded from the deltoid served as reference. The parameters in the device were set as follows: amplifier range, 500 mV; direct current time constant, 30 kHz filter; single-stimulus mode; scan speed, 10 ms/div; wave width,1 ms; stimulation frequency, 10 Hz; intensity, 10 V. The amplitude of CMEPs was quantified as the peak-to-peak amplitude, measured from the maximum positive deflection to the maximum negative deflection of the waveform.

Magnetic resonance imaging

The canine spinal cord was scanned with a 3.0 T MRI scanner (750W, GE Healthcare, USA). Animals were anesthetized with the same reagents and methods used in the surgical procedures after fasting and then positioned prone on the MRI table. To reduce motion artifacts, the heads were fixed with bite bars and ear rods. Throughout the process, an electrocardiograph monitor (MEC-1000, Mindray, China) was used for recording and monitoring respiratory rate and arterial oxygen saturation. Following the three-plane localization scanning, T1-weighted, T2-weighted and T2-FLAIR sequence images were obtained for detailed anatomical information of the spinal cord.

Diffusion tensor imaging

To assess nerve fiber regrowth at the lesion site, DTI was carried out. Spinal DTI was obtained with an SS-SE-EPI sequence and an echo time (TE) of 86.2 ms, a repetition time (TR) of 7150 ms, a field of view (FOV) of 220 mm, 50 contiguous slices, a slice thickness of 4 mm, an interslice gap of 0 mm, an acquisition matrix of 100 × 100, a voxel size of 2.2 × 2.2 × 4 mm^3, 20 diffusion-encoding directions, and a b value of 1000 s/mm^2. Raw data were imported into the commercial software 3D Slicer 5.8.1 (Kitware, USA) for processing and DTI reconstruction.

Tissue processing and histology staining

At 180 days postoperatively, the animals were euthanized and perfused with saline and 4% paraformaldehyde (PFA). The spinal cords, hearts, livers, spleens, lungs, kidneys, bladders, and gastrocnemius muscles, were collected and fixed in 4% PFA for 48 h [75].

The excised spinal cord was sequentially dehydrated in sucrose solutions of 20% and 30% at 4 °C for 24 h each. OCT compound (Sakura, Japan) was then used to embed the spinal cord, which was subsequently cryopreserved at -80 °C. The remaining tissues were prepared as paraffin blocks. Sections of all blocks were cut to a thickness of 20 μm for staining. Before all staining procedures, frozen sections were rewarmed to room temperature and rinsed in PBS for 10 min, whereas deparaffinization was applied on paraffin sections.

To observe tissues' morphology, H&E staining was conducted. Tissue sections were stained with hematoxylin (H9627, Sigma-Aldrich, USA) for a 5 min period, differentiated in acid alcohol, and counterstained in eosin (Sinopharm, China) for 2 min. Following dehydration through a graded ethanol series and clearing in xylene, the slides were coverslipped with neutral resin.

Masson staining was performed by first subjecting the tissues with Weigert's iron hematoxylin for a duration of 5 min, then briefly differentiated in 1% acid ethanol. The sections were incubated in acid fuchsin lasting 4 min, and immersed in phosphomolybdic acid solution for 5 min. The mounting steps were the same as those used for H&E staining.

For LFB staining, it was used to evaluate myelin integrity in the spinal cord. The samples were rinsed with PBS for 10 min and then immersed in LFB solution (Servicebio, China) at 60 °C for 2 h. After cooling, the tissues were rinsed successively in 95% ethanol, ultrapure water, 0.05% lithium carbonate, 70% ethanol, and ultrapure water. Finally, mounting was carried out as described above.

Immunofluorescence staining

After a 30-min blocking with goat serum, the sections were incubated overnight at 4 °C with the target primary antibody. Detailed information about the primary antibody is provided in **Table S3**. Following incubation of primary antibody, the tissues were rinsed using PBS-Tween (PBST) for 10 min, and the remaining liquid was gently removed. Fluorescent secondary antibodies (Thermo Fisher Scientific, USA) were added and then incubated for 1 h in the dark at 37 °C. The sections were then counterstained with DAPI (4',6-diamidino-2-phenylindole) lasting 5 min, rinsed with PBST for 10 min, coverslipped with anti-fading reagent, and examined with a fluorescence microscope in sequence.

For double immunofluorescence labeling, the tissue sections were blocked once more with goat serum for 30 min after the first secondary antibody incubation and washing steps were finished. The second primary antibody was then added and incubated at 4 °C overnight again, and the remaining steps were the same as those used for single labeling.

Single nuclei suspension preparation

To obtain spinal cords for single-nucleus sequencing, the canines were perfused with precooled saline immediately after euthanasia. After the vertebral laminae were exposed, the spinal cord segments containing the entire lesion site were collected and immediately instantly frozen in liquid nitrogen for subsequent processing. On account of the high value and limited availability of large-animal canines, one biologically independent canine per group was used for snRNA-seq (Uninjured, n = 1; CTRL, n = 1; INCS, n = 1).

All steps for nuclear suspension preparation were performed on ice. Spinal cords were homogenized with 1 mL of nuclear lysis buffer containing 10 mM Tris-HCl at pH 7.4, 0.1% NP-40, 1 mM $CaCl_2$, 146 mM NaCl, 1 U/μL RNase inhibitor (No. EO0382, Thermo Scientific, USA), and 21 mM $MgCl_2$, and then lysed for 7 min. Lysis was confirmed by trypan blue staining under a microscope, after which 5 mL of ST (saline-Tris) wash buffer containing 1 mM $CaCl_2$, 10 mM Tris-HCl, 21 mM $MgCl_2$, 146 mM NaCl, 0.01% BSA (No.1000076, MACS, Germany), and 40 U/mL RNase inhibitor was added. The lysate was passed through a 40 μm cell strainer into a 15 mL centrifuge tube, and the strainer was then rinsed with ST buffer. The filtrate was spun at 500 × g at 4 °C for 5 min using a swinging-bucket rotor. The nuclei were then resuspended in 5 mL of PBSB (PBS with 1% BSA) and spun under identical conditions. Following resuspending with 100 μL PBSB, nuclei concentration was determined by trypan blue staining and microscopic counting.

Single-nucleus RNA sequencing library construction

The nuclei were diluted to 1000 nuclei/μL in PBSB. Library preparation and sample loading were performed according to the manufacturer's protocol for the 10X Genomics Chromium Next GEM Single Cell 3′ Reagent Kits v3.1 (No. PN-1000268, 10X Genomics, USA). High-throughput sequencing of the libraries was conducted on a DNBSEQ-T7 platform (MGI, China). For each canine, nuclei were isolated independently and loaded into a separate 10X Genomics channel. samples were not pooled before library construction.

Single-nucleus processing and quality control

OE Biotech Co., Ltd. (Shanghai, China) performed the sequencing. Raw sequencing reads were aligned to the canine reference genome (Dog10K_Boxer_Tasha) using Cell Ranger (version 9.0.1) with the default parameters, and cell filtering and gene expression quantification were subsequently completed. The filtered feature-barcode matrices were subjected to downstream analyses.

Low-quality cells were excluded using the Seurat package (version 4.0.0) [76], and cells were kept when they satisfied the following requirements: 200 ≤ detected genes ≤ 7500; 1000 ≤ UMI (unique molecular identifier) ≤ 50 000; mitochondrial UMI content < 5%. Doublets were identified and removed with DoubletFinder (version 2.0.3) [77]. Following quality control, the retained data were normalized using the NormalizeData function.

Clustering, marker identification and cell annotation

The top 2000 highly variable genes (HVGs) were selected using the FindVariableGenes function (dispersion.function = FastLogVMR, mean.function = FastExpMean) in the Seurat package. Principal component analysis (PCA) was performed on the HVG expression profiles to reduce dimensionality, and batch effects were removed with RunHarmony in Harmony (version 1.0). The results were displayed in two-dimensional space via uniform manifold approximation and projection (UMAP).

The FindAllMarkers function (test.use = presto) in the Seurat package was used to identify marker genes, identifying genes upregulated in each cell population relative to all other populations. These genes were regarded as candidate marker genes for each cell type. The identified marker genes were visualized with VlnPlot and FeaturePlot.

Cell type annotation was based on the reference gene set (canine: Dog10K_Boxer_Tasha). Marker gene expressions were visualized for each cluster with results shown in **Figure 9 B and J**, and clusters were manually assigned to the corresponding cell types [55-59, 61, 78].

DEGs and enrichment analysis

By means of the FindMarkers function (test.use = presto), DEGs were obtained. Genes with a *P* value below 0.05 and a fold change above 1.5 were analyzed for GO and KEGG enrichment with a hypergeometric distribution test.

CellChat cell-cell communication.

Cell-cell communication analysis was performed with the CellChat R package (version 2.1.2) [79] to investigate intercellular ligand-receptor interactions. After importing the normalized gene expression matrix, a CellChat object was built via the createCellChat function. Preprocessing was then conducted with default settings using projectData identifyOverExpressedInteractions and identifyOverExpressedGenes. The functions including filterCommunication (min.cells = 10), computeCommunProbPathway and computeCommunProb, were subsequently used to compute putative ligand-receptor interactions. The aggregateNet function was applied to generate cell-cell

communication networks.

Statistical analysis

R software (version 4.0.3), GraphPad Prism 10.1.2 (GraphPad, USA) and Origin Pro 2024 (OriginLab, USA) were used for all statistical analyses and graphics. Data are shown as the mean ± SEM. The Shapiro-Wilk test was applied to evaluate the normality of the data. Comparisons among two or more groups of continuous variables with a normal distribution were made with t-tests and one-way ANOVA followed by Tukey's test. Longitudinal data were analyzed by two-way repeated-measures ANOVA followed by Šidák's multiple-comparison test. Significance was defined as $*P < 0.05$, $**P < 0.01$, $***P < 0.001$, $****P < 0.0001$. For the CMEPs and DTI examinations, three animals per group were used because of technically demanding procedures that require stringent anesthesia, precise positioning, and specialized equipment. For histological analyses, one animal per group was allocated to snRNA-seq tissue collection, the remaining five animals per group were used for histological staining.

Abbreviations

α-SMA: α-smooth muscle actin; CD68: cluster of differentiation 68; CGRP: calcitonin gene-related peptide; CMEPs: cortical motor evoked potentials; CSPG: chondroitin sulfate proteoglycans; DAPI: 4′,6-diamidino-2-phenylindole; DTI: diffusion tensor imaging; ECM: extracellular matrix; FA: fractional anisotropy; FBR: foreign body response; Fmn1: formin 1; Fn1: Fibronectin 1; H&E: hematoxylin and eosin; IBA-1: ionized calcium-binding adaptor molecule 1; LFB: Luxol fast blue; MRI: magnetic resonance imaging; NF200: neurofilament protein 200; PDGFRβ: platelet-derived growth factor receptor β; Spp1: secreted phosphoprotein 1; TH: tyrosine hydroxylase; Tktl1: transketolase-like 1; Tuj-1: neuron-specific class III β-tubulin; VEGF: vascular endothelial growth factor; 5-HT: 5-hydroxytryptamine.

Acknowledgement

This work was funded by the National Key Research and Development Program of China (2023YFC2412504), National Natural Science Foundation of China (82471424, 82071399) and Heilongjiang Provincial Natural Science Foundation of China (PL2025H128). We thanked all of the authors listed in this manuscript. We thanked Yuzhi Tan and Yaxin Fan from OE Biotech Co., Ltd (Shanghai, China) to help us with the 10X snRNA-seq.

AI usage statement

ChatGPT was used solely for language polishing and grammar correction to improve the clarity and readability. Some graphical elements in Figure 1 were generated with BioRender.com. Figure 4F was drawn by Figdraw.com. No AI tools were employed for experimental design, data collection, data analysis, or formulation of conclusions. The authors reviewed and verified all AI-assisted content, taking full responsibility for the accuracy and integrity of the manuscript.

Author Contributions

Haoxuan Huang: Writing – original draft, Data curation, Investigation, Methodology, Formal analysis. Tianqian Shen: Writing – original draft, Data curation, Investigation, Methodology, Formal analysis. Bin Dai: Methodology, Resources. Lei Wang: Investigation. Weidong Liu: Methodology. Zhaoping Wu: Data curation, Funding acquisition. Yudong Cao: Investigation. Wen Yin: Investigation. Juan Li: Methodology. Wenlong Zhang: Visualization. Caiping Ren: Writing – review and editing, Supervision, Conceptualization. Yannan Zhao: Writing – review and editing, Conceptualization, Funding acquisition, Supervision. Jianwu Dai: Writing – review and editing, Conceptualization, Funding acquisition, Supervision. Xingjun Jiang: Writing – review and editing, Conceptualization, Funding acquisition, Project administration, Supervision.

Competing interests

Co-author Bin Dai is employed by DB Wuderegen Biomedical Technologies Co., Ltd. The company holds a granted patent related to the INCS material described in this manuscript (Patent number: CN117205373B). The remaining authors declare no competing interests.

Data Availability Statement

All data supporting the conclusions of this study are provided in the main article and the accompanying supplementary materials. The snRNA-seq data in this study have been deposited in the NCBI Sequence Read Archive (SRA) under BioProject accession number PRJNA1561420. Further details can be obtained from the corresponding authors on reasonable request.

References

1. Global, regional, and national burden of spinal cord injury, 1990-2019: a systematic analysis for the Global Burden of Disease Study 2019. Lancet Neurol. 2023; 22: 1026-47.
2. Dietz V, Fouad K. Restoration of sensorimotor functions after spinal cord injury. Brain. 2014; 137: 654-67.
3. Tang F, Tang J, Zhao Y, Zhang J, Xiao Z, Chen B, et al. Long-term clinical observation of patients with acute and chronic complete spinal cord injury after transplantation of NeuroRegen scaffold. Sci China Life Sci. 2022; 65: 909-26.
4. Xiao Z, Tang F, Tang J, Yang H, Zhao Y, Chen B, et al. One-year clinical study of NeuroRegen scaffold implantation following scar resection in complete chronic spinal cord injury patients. Sci China Life Sci. 2016; 59: 647-55.
5. Brown AR, Martinez M. From cortex to cord: motor circuit plasticity after spinal cord injury. Neural Regen Res. 2019; 14: 2054-62.
6. Ahuja CS, Nori S, Tetreault L, Wilson J, Kwon B, Harrop J, et al. Traumatic Spinal Cord Injury-Repair and Regeneration. Neurosurgery. 2017; 80: S9-s22.
7. Hu X, Xu W, Ren Y, Wang Z, He X, Huang R, et al. Spinal cord injury: molecular mechanisms and therapeutic interventions. Signal Transduct Target Ther. 2023; 8: 245.
8. Patel M, Deng AJ, Hasoon J, Wahezi S, Abd-Elsayed A. A Review of Pathophysiology, Molecular Mechanisms, and Omics Approaches of Spinal Cord Injury. Int J Mol Sci. 2025; 26.
9. Ma D, Fu C, Li F, Ruan R, Lin Y, Li X, et al. Functional biomaterials for modulating the dysfunctional pathological microenvironment of spinal cord injury. Bioact Mater. 2024; 39: 521-43.
10. Haratizadeh S, Liu H, Li H, Adeli M, All AH. Biomaterials and cell-based therapy post spinal cord injury. J Transl Med. 2025; 23: 1042.
11. Tan Z, Xiao L, Ma J, Shi K, Liu J, Feng F, et al. Integrating hydrogels manipulate ECM deposition after spinal cord injury for specific neural reconnections via neuronal relays. Sci Adv. 2024; 10: eado9120.
12. Feng F, Song X, Tan Z, Tu Y, Xiao L, Xie P, et al. Cooperative assembly of a designer peptide and silk fibroin into hybrid nanofiber gels for neural regeneration after spinal cord injury. Sci Adv. 2023; 9: eadg0234.
13. Brown M, Li J, Moraes C, Tabrizian M, Li-Jessen NYK. Decellularized extracellular matrix: New promising and challenging biomaterials for regenerative medicine. Biomaterials. 2022; 289: 121786.
14. Zhu L, Yuhan J, Yu H, Zhang B, Huang K, Zhu L. Decellularized Extracellular Matrix for Remodeling Bioengineering Organoid's Microenvironment. Small. 2023; 19: e2207752.
15. Sun Z, Chen Z, Yin M, Wu X, Guo B, Cheng X, et al. Harnessing developmental dynamics of spinal cord extracellular matrix improves regenerative potential of spinal cord organoids. Cell Stem Cell. 2024; 31: 772-87.e11.
16. Hong JY, Seo Y, Davaa G, Kim HW, Kim SH, Hyun JK. Decellularized brain matrix enhances macrophage polarization and functional improvements in rat spinal cord injury. Acta Biomater. 2020; 101: 357-71.
17. Cerqueira SR, Lee YS, Cornelison RC, Mertz MW, Wachs RA, Schmidt CE, et al. Decellularized peripheral nerve supports Schwann cell transplants and axon growth following

spinal cord injury. Biomaterials. 2018; 177: 176-85.
18. Jiang W, Zhang X, Yu S, Yan F, Chen J, Liu J, et al. Decellularized extracellular matrix in the treatment of spinal cord injury. Exp Neurol. 2023; 368: 114506.
19. Chaudhari LR, Kawale AA, Shinde CN, Neglur PK, Sonkawade O, Patil J, et al. Perfusion-Decellularized Goat Spinal Cord Scaffold Promotes Neuroregeneration and Functional Recovery in a Rat Model of Spinal Cord Injury. J Biomed Mater Res B Appl Biomater. 2026; 114: e70031.
20. Verstappen K, Klymov A, Cicuéndez M, da Silva DM, Barroca N, Fernández-San-Argimiro FJ, et al. Biocompatible adipose extracellular matrix and reduced graphene oxide nanocomposite for tissue engineering applications. Mater Today Bio. 2024; 26: 101059.
21. Xu Y, Zhou J, Liu C, Zhang S, Gao F, Guo W, et al. Understanding the role of tissue-specific decellularized spinal cord matrix hydrogel for neural stem/progenitor cell microenvironment reconstruction and spinal cord injury. Biomaterials. 2021; 268: 120596.
22. Walsh CM, Wychowaniec JK, Brougham DF, Dooley D. Functional hydrogels as therapeutic tools for spinal cord injury: New perspectives on immunopharmacological interventions. Pharmacol Ther. 2022; 234: 108043.
23. Sun Y, Yang C, Zhu X, Wang JJ, Liu XY, Yang XP, et al. 3D printing collagen/chitosan scaffold ameliorated axon regeneration and neurological recovery after spinal cord injury. J Biomed Mater Res A. 2019; 107: 1898-908.
24. Liu D, Niu R, Wang S, Shao L, Yang X, Liu X, et al. Nitric Oxide-Releasing Mesoporous Hollow Cerium Oxide Nanozyme-Based Hydrogel Synergizes with Neural Stem Cell for Spinal Cord Injury Repair. ACS Nano. 2025; 19: 2591-614.
25. Bailly N, Wagnac E, Petit Y. Regional mechanical properties of spinal cord gray and white matter in transverse section. J Mech Behav Biomed Mater. 2025; 163: 106898.
26. Han S, Li X, Xiao Z, Dai J. Complete canine spinal cord transection model: a large animal model for the translational research of spinal cord regeneration. Sci China Life Sci. 2018; 61: 115-7.
27. Liu D, Li X, Xiao Z, Yin W, Zhao Y, Tan J, et al. Different functional bio-scaffolds share similar neurological mechanism to promote locomotor recovery of canines with complete spinal cord injury. Biomaterials. 2019; 214: 119230.
28. Li X, Zhao Y, Cheng S, Han S, Shu M, Chen B, et al. Cetuximab modified collagen scaffold directs neurogenesis of injury-activated endogenous neural stem cells for acute spinal cord injury repair. Biomaterials. 2017; 137: 73-86.
29. Han S, Wang B, Jin W, Xiao Z, Li X, Ding W, et al. The linear-ordered collagen scaffold-BDNF complex significantly promotes functional recovery after completely transected spinal cord injury in canine. Biomaterials. 2015; 41: 89-96.
30. Wen R, Long G, He X, Zhang K, Ma W, Shen Y, et al. Revisiting the unobtrusive role of exogenous stem cells beyond neural circuits replacement in spinal cord injury repair. Theranostics. 2025; 15: 1552-69.
31. Courtine G, Bunge MB, Fawcett JW, Grossman RG, Kaas JH, Lemon R, et al. Can experiments in nonhuman primates expedite the translation of treatments for spinal cord injury in humans? Nat Med. 2007; 13: 561-6.
32. Yin W, Li X, Zhao Y, Tan J, Wu S, Cao Y, et al. Taxol-modified collagen scaffold implantation promotes functional recovery after long-distance spinal cord complete transection in canines.

Biomater Sci. 2018; 6: 1099-108.
33. Olby NJ, De Risio L, Muñana KR, Wosar MA, Skeen TM, Sharp NJ, et al. Development of a functional scoring system in dogs with acute spinal cord injuries. Am J Vet Res. 2001; 62: 1624-8.
34. Harrigan ME, Filous AR, Vadala CP, Webb A, Pietrzak M, Sahenk Z, et al. Lesion level-dependent systemic muscle wasting after spinal cord injury is mediated by glucocorticoid signaling in mice. Sci Transl Med. 2023; 15: eadh2156.
35. Xie L, Liu D, Liu Z, Wang Y, Zhang H, Zhuang J, et al. Immuno-Neuroprotectants Facilitate Neurological Recovery via Sequestration of Neutrophil Extracellular Traps (NETs) and Promotion of Neuroregeneration. Adv Mater. 2026; 38: e18580.
36. Zhang D, Zhou X, Zhao C, Han S, Guo X, Chen H, et al. Spatiotemporal-controlled ultrasound-driven Li-PDA@ZnO nanoparticles promote neural stem cell differentiation synergy with biohydrogel repair spinal cord injury. Bioact Mater. 2026; 55: 446-63.
37. Wang H, Hu H, Li Y, Hu L, Gu C, Zhu Y, et al. A Conjugation Delivery System of Macrophages and Platelet Pharmacytes Promotes Regeneration After Spinal Cord Injury. Adv Sci (Weinh). 2026; 13: e13474.
38. Su X, Gu C, Wei Z, Sun Y, Zhu C, Chen X. Chitosan-Modified Hydrogel Microsphere Encapsulating Zinc-Doped Bioactive Glasses for Spinal Cord Injury Repair by Suppressing Inflammation and Promoting Angiogenesis. Adv Healthc Mater. 2025; 14: e2402129.
39. Sąsiadek MJ, Szewczyk P, Bladowska J. Application of diffusion tensor imaging (DTI) in pathological changes of the spinal cord. Med Sci Monit. 2012; 18: Ra73-9.
40. Vedantam A, Jirjis MB, Schmit BD, Wang MC, Ulmer JL, Kurpad SN. Diffusion tensor imaging of the spinal cord: insights from animal and human studies. Neurosurgery. 2014; 74: 1-8; discussion ; quiz
41. Wang-Leandro A, Hobert MK, Kramer S, Rohn K, Stein VM, Tipold A. The role of diffusion tensor imaging as an objective tool for the assessment of motor function recovery after paraplegia in a naturally-occurring large animal model of spinal cord injury. J Transl Med. 2018; 16: 258.
42. Shimizu N, Saito T, Wada N, Hashimoto M, Shimizu T, Kwon J, et al. Molecular Mechanisms of Neurogenic Lower Urinary Tract Dysfunction after Spinal Cord Injury. Int J Mol Sci. 2023; 24.
43. Veiseh O, Vegas AJ. Domesticating the foreign body response: Recent advances and applications. Adv Drug Deliv Rev. 2019; 144: 148-61.
44. Gong L, Gu Y, Han X, Luan C, Liu C, Wang X, et al. Spatiotemporal Dynamics of the Molecular Expression Pattern and Intercellular Interactions in the Glial Scar Response to Spinal Cord Injury. Neurosci Bull. 2023; 39: 213-44.
45. Xiao L, Shi K, Li W, Liu J, Xie P, Hu Z, et al. Targeting Fibrotic Scarring by Mechanoregulation of Il11ra1(+)/Itga11(+) Fibroblast Patterning Promotes Axon Growth after Spinal Cord Injury. Adv Sci (Weinh). 2025; 12: e13476.
46. Zhou X, Wahane S, Friedl MS, Kluge M, Friedel CC, Avrampou K, et al. Microglia and macrophages promote corralling, wound compaction and recovery after spinal cord injury via Plexin-B2. Nat Neurosci. 2020; 23: 337-50.
47. Li C, Xiong W, Wan B, Kong G, Wang S, Wang Y, et al. Role of peripheral immune cells in spinal cord injury. Cell Mol Life Sci. 2022; 80: 2.

48. Jin LY, Li J, Wang KF, Xia WW, Zhu ZQ, Wang CR, et al. Blood-Spinal Cord Barrier in Spinal Cord Injury: A Review. J Neurotrauma. 2021; 38: 1203-24.
49. Shibahara T, Nakamura K, Wakisaka Y, Shijo M, Yamanaka K, Takashima M, et al. PDGFRβ-positive cell-mediated post-stroke remodeling of fibronectin and laminin α2 for tissue repair and functional recovery. J Cereb Blood Flow Metab. 2023; 43: 518-30.
50. Dias DO, Göritz C. Fibrotic scarring following lesions to the central nervous system. Matrix Biol. 2018; 68-69: 561-70.
51. Hellenbrand DJ, Quinn CM, Piper ZJ, Morehouse CN, Fixel JA, Hanna AS. Inflammation after spinal cord injury: a review of the critical timeline of signaling cues and cellular infiltration. J Neuroinflammation. 2021; 18: 284.
52. Bellver-Landete V, Bretheau F, Mailhot B, Vallières N, Lessard M, Janelle ME, et al. Microglia are an essential component of the neuroprotective scar that forms after spinal cord injury. Nat Commun. 2019; 10: 518.
53. Zheng B, Tuszynski MH. Regulation of axonal regeneration after mammalian spinal cord injury. Nat Rev Mol Cell Biol. 2023; 24: 396-413.
54. Walters ET. How is chronic pain related to sympathetic dysfunction and autonomic dysreflexia following spinal cord injury? Auton Neurosci. 2018; 209: 79-89.
55. Skinnider MA, Gautier M, Teo AYY, Kathe C, Hutson TH, Laskaratos A, et al. Single-cell and spatial atlases of spinal cord injury in the Tabulae Paralytica. Nature. 2024; 631: 150-63.
56. Fan Y, Wu X, Han S, Zhang Q, Sun Z, Chen B, et al. Single-cell analysis reveals region-heterogeneous responses in rhesus monkey spinal cord with complete injury. Nat Commun. 2023; 14: 4796.
57. Matson KJE, Russ DE, Kathe C, Hua I, Maric D, Ding Y, et al. Single cell atlas of spinal cord injury in mice reveals a pro-regenerative signature in spinocerebellar neurons. Nat Commun. 2022; 13: 5628.
58. Milich LM, Choi JS, Ryan C, Cerqueira SR, Benavides S, Yahn SL, et al. Single-cell analysis of the cellular heterogeneity and interactions in the injured mouse spinal cord. J Exp Med. 2021; 218.
59. Li C, Wu Z, Zhou L, Shao J, Hu X, Xu W, et al. Temporal and spatial cellular and molecular pathological alterations with single-cell resolution in the adult spinal cord after injury. Signal Transduct Target Ther. 2022; 7: 65.
60. Song Y, Luengo-Gutierrez L, Sagi-Kiss V, Kong G, Huang H, Steinruecke M, et al. A glycolytic shunt via the pentose phosphate pathway is a metabolic checkpoint for nervous system sensory homeostasis and axonal regeneration. Cell. 2026; 189: 1211-27.e25.
61. Li Y, He X, Kawaguchi R, Zhang Y, Wang Q, Monavarfeshani A, et al. Microglia-organized scar-free spinal cord repair in neonatal mice. Nature. 2020; 587: 613-8.
62. Fang YP, Qin ZH, Zhang Y, Ning B. Implications of microglial heterogeneity in spinal cord injury progression and therapy. Exp Neurol. 2023; 359: 114239.
63. Wang X, Zhou G, Xiong J, Ye W, Gao Y, Wang H, et al. H4K12 Lactylation Activated-Spp1 in Reprogrammed Microglia Improves Functional Recovery After Spinal Cord Injury. CNS Neurosci Ther. 2025; 31: e70232.
64. Qiu Y, Shen X, Ravid O, Atrakchi D, Rand D, Wight AE, et al. Definition of the contribution of an Osteopontin-producing CD11c(+) microglial subset to Alzheimer's disease. Proc Natl Acad Sci U S A. 2023; 120: e2218915120.

65. Shi L, Sun Z, Su W, Xu F, Xie D, Zhang Q, et al. Treg cell-derived osteopontin promotes microglia-mediated white matter repair after ischemic stroke. Immunity. 2021; 54: 1527-42.e8.
66. Liu J, Yao Z, Hu Z, Zhang X, Gong B, Dai Y, et al. Spatiotemporal Delivery of Required Facilitators for Microenvironment Remodeling Propels Neural Regeneration after Spinal Cord Injury. Adv Mater. 2026; 38: e03479.
67. Wang G, Li Q, Liu S, Li M, Liu B, Zhao T, et al. An injectable decellularized extracellular matrix hydrogel with cortical neuron-derived exosomes enhances tissue repair following traumatic spinal cord injury. Mater Today Bio. 2024; 28: 101250.
68. Yin W, Xue W, Zhu H, Shen H, Xiao Z, Wu S, et al. Scar tissue removal-activated endogenous neural stem cells aid Taxol-modified collagen scaffolds in repairing chronic long-distance transected spinal cord injury. Biomater Sci. 2021; 9: 4778-92.
69. Wu Z, Zhou Y, Hou X, Liu W, Yin W, Wang L, et al. Construction of functional neural network tissue combining CBD-NT3-modified linear-ordered collagen scaffold and TrkC-modified iPSC-derived neural stem cells for spinal cord injury repair. Bioact Mater. 2024; 35: 242-58.
70. Liu W, Xu B, Xue W, Yang B, Fan Y, Chen B, et al. A functional scaffold to promote the migration and neuronal differentiation of neural stem/progenitor cells for spinal cord injury repair. Biomaterials. 2020; 243: 119941.
71. Liu J, Yan R, Wang B, Chen S, Hong H, Liu C, et al. Decellularized extracellular matrix enriched with GDNF enhances neurogenesis and remyelination for improved motor recovery after spinal cord injury. Acta Biomater. 2024; 180: 308-22.
72. Saliani A, Perraud B, Duval T, Stikov N, Rossignol S, Cohen-Adad J. Axon and Myelin Morphology in Animal and Human Spinal Cord. Front Neuroanat. 2017; 11: 129.
73. Quan R, Hou X, Zhang J, Chen Z, Liu W, Guo B, et al. Spatiotemporally Engineered Protein Delivery via Integrated Covalent Coupling and Pathological Triggers for Precision Microenvironment Reprogramming in Tissue Injury Repair. Adv Mater. 2026; 38: e12554.
74. Webb AA, Jeffery ND, Olby NJ, Muir GD. Behavioural analysis of the efficacy of treatments for injuries to the spinal cord in animals. Vet Rec. 2004; 155: 225-30.
75. Cao Z, Man W, Xiong Y, Guo Y, Yang S, Liu D, et al. White matter regeneration induced by aligned fibrin nanofiber hydrogel contributes to motor functional recovery in canine T12 spinal cord injury. Regen Biomater. 2022; 9: rbab069.
76. Hao Y, Hao S, Andersen-Nissen E, Mauck WM, 3rd, Zheng S, Butler A, et al. Integrated analysis of multimodal single-cell data. Cell. 2021; 184: 3573-87.e29.
77. McGinnis CS, Murrow LM, Gartner ZJ. DoubletFinder: Doublet Detection in Single-Cell RNA Sequencing Data Using Artificial Nearest Neighbors. Cell Syst. 2019; 8: 329-37.e4.
78. Saraswathy VM, Zhou L, Mokalled MH. Single-cell analysis of innate spinal cord regeneration identifies intersecting modes of neuronal repair. Nat Commun. 2024; 15: 6808.
79. Jin S, Guerrero-Juarez CF, Zhang L, Chang I, Ramos R, Kuan CH, et al. Inference and analysis of cell-cell communication using CellChat. Nat Commun. 2021; 12: 1088.